



**HAL**  
open science

## The deformed alkaline Balda granite (Northern Cameroon): A witness of back-arc basin in the northern part of Central African Orogenic Belt

Aboubakar Bello, Daouda Dawai, Paul Yves Jean Antonio, Oscar Laurent, Carmen Irene Martinez Dopico, Rigobert Tchameni, Olivier Vanderhaeghe

### ► To cite this version:

Aboubakar Bello, Daouda Dawai, Paul Yves Jean Antonio, Oscar Laurent, Carmen Irene Martinez Dopico, et al.. The deformed alkaline Balda granite (Northern Cameroon): A witness of back-arc basin in the northern part of Central African Orogenic Belt. *Precambrian Research*, 2024, 410, pp.107490. 10.1016/j.precamres.2024.107490 . hal-04751379

**HAL Id: hal-04751379**

**<https://hal.science/hal-04751379v1>**

Submitted on 20 Nov 2024

**HAL** is a multi-disciplinary open access archive for the deposit and dissemination of scientific research documents, whether they are published or not. The documents may come from teaching and research institutions in France or abroad, or from public or private research centers.

L'archive ouverte pluridisciplinaire **HAL**, est destinée au dépôt et à la diffusion de documents scientifiques de niveau recherche, publiés ou non, émanant des établissements d'enseignement et de recherche français ou étrangers, des laboratoires publics ou privés.

1 **The deformed alkaline Balda granite (Northern Cameroon): a witness of back-arc basin in**  
2 **the northern part of Central African Orogenic Belt**

3 Aboubakar Bello<sup>a</sup>, Daouda Dawai<sup>a</sup>, Paul Yves Jean Antonio<sup>b,c</sup>, Oscar Laurent<sup>d</sup>, Carmen Irene  
4 Martinez Dopico<sup>b</sup>, Rigobert Tchameni<sup>e</sup>, Olivier Vanderhaeghe<sup>d</sup>

5 <sup>a</sup> Department of Earth Sciences, Faculty of Sciences, University of Maroua, PO Box 814, Maroua,  
6 Cameroon

7 <sup>b</sup> Géosciences Montpellier, UMR 5243, Université de Montpellier, 34095, Montpellier, France

8 <sup>c</sup> Centre for Planetary Habitability, University of Oslo, Oslo, Norway

9 <sup>d</sup> Géosciences Environnement Toulouse, Observatoire Midi-Pyrénées, Université Toulouse III-Paul  
10 Sabatier, CNRS, IRD, 31400, Toulouse Cedex, France

11 <sup>e</sup> Department of Earth Sciences, Faculty of Sciences, University of Ngaoundéré, PO Box 454,  
12 Ngaoundéré, Cameroon

13 **Abstract**

14 Located on the border between the NW Cameroon and Mayo-Kebbi domains in northern  
15 Cameroon, the Balda pluton is a deformed alkaline granite. Due to its unique location and  
16 geological features, it holds crucial information for understanding the evolution of the  
17 Central African Orogenic Belt (CAOB), which remains poorly understood. This  
18 multidisciplinary study combines field data, microscopic observations, Anisotropy of  
19 Magnetic Susceptibility (AMS), and U-Pb zircon dating to constrain the geodynamic  
20 evolution of the CAOB.

21 The Balda pluton is a NNE-SSW elongated pluton consists mainly of aegirine-riebeckite  
22 granite and leucogranite. It displays diverse magnetic susceptibility values (Km) spanning  
23 from  $0.19 \times 10^{-3}$  to  $21.98 \times 10^{-3}$ . Notably, 93% of the Km values exceed  $5 \times 10^{-4}$  SI,

24 indicating a prevalence of mixed paramagnetic and ferromagnetic mineralogy (such as  
25 magnetite-rich). This observation is supported by microscopic examinations and K-T curves.  
26 An analysis of AMS unveils high P% values (2.8 to 58.7 %, with a mean of 15 %) and  
27 prevalent oblate magnetic fabrics (68%). The magnetic foliation generally aligns with the  
28 field foliation and has steep dips ranging from NNE to NE or from SSW to SW and magnetic  
29 lineations exhibit shallow plunges (<35°) from SSW to SW. Microscopic analysis reveals  
30 high-temperature, solid-state deformation microstructures, indicating post-emplacment  
31 deformation processes and the presence of kinematic markers consistent with sinistral  
32 shear. Zircon grain analysis reveals two distinct types: "bright" and "dark." These types  
33 differ in both their appearance under cathodoluminescence and their chemical  
34 composition. Bright zircons yield a U-Pb age of  $732.7 \pm 7.5$  Ma, interpreted as the pluton  
35 emplacement age. Dark zircons are younger (ca. 680 Ma), suggesting a later tectono-  
36 metamorphic or alteration event.

37 The integration of these results in a larger geodynamic context suggests that the Balda  
38 pluton formed within a syn-orogenic extensional back-arc basin. This emplacement was  
39 followed by significant post-emplacment deformation characterized by sinistral simple  
40 shear-dominated transpression likely related to the continental collision (ca. 680 Ma) of the  
41 NW Cameroon and Mayo-Kébbi domains.

42 Keywords: CAOB, Balda pluton, U-Pb zircon dating, AMS, post-emplacment deformation,  
43 back-arc basin.

44

45

47 **1. Introduction**

48 The Central African Orogenic Belt (CAOB), extending northward of the Congo Craton, is  
49 composed of a set of geological domains or microcontinents that were accreted as a result  
50 of the convergence and collision between the Congo Craton, West African Craton, and  
51 Saharan Metacraton (Fig. 1a &b) between 790 and 500 Ma during the assembly of the  
52 Gondwana supercontinent (Ferré et al., 2002; Toteu et al., 2004; Ngako et al., 2008; Van  
53 Schmus et al., 2008). The CAOB is part of the major West Gondwana Orogen, a linear belt  
54 that stretches for more than ~4000 km between South America and central Africa marking  
55 the closure of the Goiás-Pharusian Ocean (Hurley et al., 1967; Caby, 1989; Trompette,  
56 1994, 1997; Brito Neves et al., 2002; Oliveira et al., 2006, Arthaud et al., 2008; Dada, 2008;  
57 Van Schmus et al., 2008; Ganade de Araújo et al., 2014, 2016; Caxito et al., 2020). On the  
58 other hand, the continuation of the CAOB to the east and its relationship with the southern  
59 and eastern margins of the Saharan Metacraton remain uncertain (Toteu et al., 2022;  
60 Djerosse et al., 2020). Indeed, the eastern part of the CAOB is divided into two branches  
61 with the NS Western African Orogen to the north and the EW Central African Orogen (De  
62 Wit et al., 2008; Caxito et al., 2020; Toteu et al., 2022). Therefore, the northernmost part of  
63 the CAOB at the Cameroon-Chad-Nigeria junction represents a key area to understand this  
64 enigmatic connection between the Congo craton and the Sahara Metacraton in Central  
65 Africa.

66 Currently, the proposed model for the geology of this area (Penaye et al., 2006; Pouclet  
67 et al., 2006) suggests that the current configuration of these domains results from a Pan-  
68 African tectonic collage of microcontinents preceded by subduction, followed by suturing

69 of the oceanic crust. However, this model remains uncertain owing to the lack of witnesses  
70 of ocean closure (*e.g.*, ophiolite evidence). The suture zones are key markers for  
71 paleocontinent reconstruction studies (Dilek and Furnes, 2014; Sehsah et al., 2019) and  
72 favorable settings for ore deposit exploration (Groves et al., 2018; Pirajno et al., 2020).  
73 Therefore, it is essential to bring new arguments for consideration of the geodynamic  
74 model currently proposed for the northern part of the CAO B.

75 The Balda granite pluton located in the northern extension of the assumed suture zone  
76 (Fig. 1c) is identified as deformed alkaline granite (Dumort and Peronne, 1966). Such rocks  
77 can be associated with ophiolitic plate suture zones and are interpreted as relics of the  
78 crustal rifting stage subsequently deformed by continental collision (Burke et al., 2003,  
79 2008; Burke and Khan, 2006; Leelanandam et al., 2006; Ashwal et al., 2007; Nanda et al.,  
80 2009). Therefore, they may be regarded as potential indicators of ancient suture zones.  
81 However, other studies have revealed that the emplacement of these rocks can also be  
82 related to orogenic processes, such as local syn-orogenic extension contexts (Attoh et al.,  
83 2007; Sokol et al., 2018; Sheikh et al., 2020) and strike-slip shear regimes that follow  
84 collision (Liègeois and Black, 1987; Bonin, 1990; Archanjo and Bouchez, 1997; Nsifa et al.,  
85 2013; Valentin et al., 2020). To constrain their geotectonic significance, it is essential to  
86 decipher the time relationship between fabric development in these granites and regional  
87 tectonics.

88 In this contribution, we present the results of a multidisciplinary study, including field  
89 and microscopic observations, Anisotropy of Magnetic Susceptibility (AMS) analysis, and  
90 zircons composition and U-Pb geochronology of the Balda granitic pluton. Our aims are to  
91 (1) constrain the emplacement age; (2) evaluate the structural patterns of intrusion in  
92 relation to regional tectonics and timing of deformation; and (3) provide further insight

93 into the geodynamic evolution of the northern margin of the Central African Orogenic Belt  
94 in relation to its transatlantic connection with the Brazilian Borborema Province.

95

## 96 **2. Regional geology**

97 The CAOB outcrops in Nigeria, Cameroon, Chad, and Central African Republic. In its  
98 northern part, it is subdivided into different geological domains, from south to northwest:  
99 the Adamawa-Yadé, the Mayo-Kébbi, and the North-West Cameroon domains (Fig. 1c).

100 The Adamawa-Yadé, also known as the Central Cameroon domain, consists mainly of (i)  
101 migmatitic gneisses with Paleoproterozoic and Archean inheritance (Saha- Fouotsa et al.,  
102 2019) revealed by inherited zircon and Nd isotope data, (ii) Neoproterozoic  
103 metasedimentary rocks (Soba et al., 1991; Toteu et al., 2006) intruded by (iii) successive  
104 generations of Pan-African granitoids (Tchameni et al., 2006; Fotso et al., 2022). These  
105 granitoids are categorized as pre-, syn-, late- or post-tectonic, with reference to their state  
106 of deformation. This domain is marked by the late Pan-African shear zone system, called  
107 the Central Cameroon Shear zone (CCSZ; Fig. 1c; Ngako et al., 1991; Njonfang et al., 2006).  
108 This tectonic structure has played an active role in the emplacement of numerous granitic  
109 intrusions of the domain (Dawai et al., 2017; Bella Nké et al., 2018). The Adamawa-Yadé  
110 domain is considered as an Archean domain reworked by successive Paleoproterozoic and  
111 Neoproterozoic orogenies (Toteu et al., 2001, 2004; Penaye et al., 2004; Ganwa et al.,  
112 2016; Saha-Fouotsa et al., 2019). It has been interpreted by Tchakounté et al. (2017) as a  
113 detached piece from the northern margin of the Archean Congo Craton in the early  
114 Neoproterozoic, and then re-accreted with the Mayo-Kébbi (magmatic) arc during the Pan-  
115 African orogeny.

116 The Mayo-Kébbi domain is located in the southwestern part of Chad and extends locally to  
117 northeast Cameroon (Fig. 1c). Geologically, it is sandwiched between the Adamawa-Yade  
118 domain to the southeast and North-West Cameroon domain to the northeast (Fig. 1c). It is  
119 distinguished from these two domains by its crustal composition, predominately  
120 Neoproterozoic, juvenile and early magmatism (ca. 740 Ma) (Penaye et al., 2006; Pouclet et  
121 al., 2006; Isseini, 2011). It comprises (1) greenstone belts represented by two narrow and  
122 NNE-SSW elongate series bordering the domain in the east and west. Lithologically, they  
123 are composed of mafic metaplutonic and metavolcanic rocks associated with  
124 metasedimentary rocks and metavolcaniclastics (Kasser 1995; Doumnang, 2006; Pouclet et  
125 al. 2006; Isseini 2011); (2) a calc-alkaline magmatic suite (Wacrenier, 1962; Kasser, 1998;  
126 Doumnang, 2006; Penaye et al. 2006; Pouclet et al., 2006), and some rare alkaline  
127 intrusions (Basua et al., 2022) were emplaced in the greenstone belts between 737 and 638  
128 Ma (Penaye et al., 2006; Isseini, 2011); and (3) a high-K magmatic suite dated between 582  
129 and 570 Ma (Penaye et al., 2006; Pouclet et al., 2006; Isseini et al., 2012; Couzinié et al.,  
130 2020), which hosts uranium deposits (Vanderhaeghe et al., 2020). This domain is  
131 recognized as a long-lived accretionary orogen formed during the time-span of 800-550 Ma  
132 by successive convergence with the Adamawa-Yadé and North-West Cameroon domains  
133 (Penaye et al., 2006; Pouclet et al., 2006; Isseini, 2011; Bouyo Houketchang et al., 2016).

134 The North-West Cameroon domain (NWCD), also called the North Cameroon domain, is  
135 bounded by the Tcholliré-Banyo Shear zone to the far southeast (Toteu et al., 2004; Nomo  
136 Negue et al., 2017) and by the Poli-Léré-Maroua (Fig. 1c) volcano-sedimentary belt to the  
137 east (Bouyo Houketchang et al., 2016). These separate it from the Adamawa-Yadé and  
138 Mayo-Kebbi domains, respectively (Fig. 1c; Toteu et al., 2004; Van Schmus et al., 2008). The  
139 isotopic data (Rb-Sr and Sm-Nd) suggest that most of the rocks in this domain are juvenile

140 Neoproterozoic rocks or contaminated by Paleoproterozoic components, but without  
141 Archean materials in the source (Toteu et al., 2001) is considered by Ferré et al. (1996,  
142 2002) as the eastward extension of the East Nigerian domain. To the north, its relationship  
143 with the Sahara Metacraton remains controversial (Abdelsalam et al., 2002; Liégeois et al.,  
144 2013; Shellnutt et al., 2019; Djerosse et al., 2020). The NWCD is separated by the Benue  
145 Trough into Southern and Northern parts, which is a Cretaceous rift (Guiraud, 1990). The  
146 southern part is dominated by the Poli group (Toteu et al., 2006). The latter is a pre- to syn-  
147 collisional basin deposited in a magmatic arc context, deformed and metamorphosed  
148 during the Pan-African orogeny (Toteu et al., 2006). It consists of gneissic rocks and  
149 medium-to high-grade schists of volcanic to volcano-sedimentary origin characterized by U-  
150 Pb detrital zircon ages ranging from 920 to 730 Ma and depositional ages constrained  
151 between 700 and 665 Ma (Toteu et al., 2006, 2022; Bouyo Houketchang et al., 2009).  
152 Similar rocks have been locally reported in the northern part of the NWCD (Schwoerer,  
153 1965; Dumort and Peronne, 1966).

154 At the scale of the entire NWCD, geological, geochemical, and geochronological studies  
155 indicate that the gneiss and volcano-sedimentary rocks were intruded by three generations  
156 of calc-alkaline to alkaline intrusive rocks during the Cryogenian to Ediacarian period. These  
157 intrusions are classified according to their structural features as pre-tectonic (670-630 Ma),  
158 syn- to late-tectonic (600-580 Ma), and post-tectonic (540 Ma) (Toteu et al., 2001, 2004;  
159 Dawai et al., 2013; Tchameni et al., 2016; Fosso Tchunte et al., 2018; Sep Nlomngan et al.,  
160 2021).

161 The tectonic history recorded by the NWCD is summarized in two stages of deformation  
162 (Dumont et al., 1985; Nzenti et al., 1992; Ngako et al., 2003, 2008; Toteu et al., 2004; Dawai  
163 et al., 2013; Sep Nlomngan et al., 2021). The first stage is characterized by sub-horizontal

164 foliation associated with isoclinal folds and N110°E–140°E stretching lineations, which are  
165 locally well-preserved. The second stage is marked by tight and upright folds associated  
166 with vertical and NNE-trending foliation. This foliation carries a mineral lineation parallel to  
167 the fold axes, oriented NNE-SSW to NE-SW and dipping 0° to 50° to the south or north.

### 168 **3. Field descriptions and petrography**

169 The Balda pluton is located approximately 45 km northeast of Maroua town (Fig. 1c), the  
170 capital of the Cameroon Far-North region. It occurs as a small and elongated NNE-SSW  
171 intrusive body approximately 5 km long and 0.5-2 km wide for an area of  $\approx 4 \text{ km}^2$  (Fig. 2). It  
172 constitutes a mountain of moderate elevation, culminating at 580 m above the  $\sim 330 \text{ m}$ -  
173 high Diamaré Plain, commonly with steep flanks (Fig. 3a). The massif crops out as slabs or  
174 boulders (Fig. 3b) with widely variable sizes and is frequently cross-cut by 2 to 10 cm wide  
175 quartz veins (Fig. 3c). The host rocks of the pluton are not observable because of the thick  
176 post-Pan-African deposits that completely cover them. Similarly, no xenoliths of the host  
177 rock were observed.

178 The Balda pluton is made of granitic rocks that vary in composition from aegirine-riebeckite  
179 granite to leucogranite. The aegirine-riebeckite granite is the most abundant facies ( $\sim 80\%$   
180 of the outcrops). It is medium-grained with slight variation in grain size throughout the  
181 outcrops and grey to grey light in color (Fig. 3 d&e). The leucogranite is medium-grained  
182 and light grey to white in color (Fig. 3f). It is mainly located at the NNE end of the outcrops.  
183 The transition between both facies is progressive. Therefore, the rock color variations seem  
184 to be linked to changes in the modal whole-rock compositions.

185 These granitic rocks display a mesoscopic foliation devoid of a lineation. This foliation,  
186 which is underlined by biotite and flattened quartz grains, is preferentially oriented to NNE-

187 SSW (Fig. 3d). In the core of the pluton, the fabric is discreetly expressed or not visible (Fig.  
188 3e).

189 Microscopic investigation reveals that the aegirine-riebeckite granite has a heterogranular  
190 texture (Fig. 4 a&b) and is composed, in order of volumetric proportion, of quartz, K-  
191 feldspar, plagioclase, aegirine, riebeckite and biotite. Accessory minerals are oxides,  
192 apatite, zircon, and allanite. Quartz occurs as anhedral crystals with sizes ranging from 1 to  
193 3 mm, displaying undulose extinction. Recrystallized quartz grains are also present around  
194 large crystals of quartz or feldspar. K-feldspar is mainly microcline. It occurs as subhedral  
195 grains of variable size (0.4- 3 mm). Some crystals intergrew with plagioclase crystals,  
196 forming a perthitic texture (Fig. 4c). Plagioclase appears as small subhedral grains (~ 0.4 - 3  
197 mm). Both types of feldspars are sometimes poikilitic and contain small quartz grains. Fe-  
198 Mg silicates are often spatially associated with opaque minerals. Biotite is generally  
199 subhedral with reddish-brown to brown pleochroism and is partially retrogressed to  
200 chlorite. In foliated rocks, biotite and opaque minerals are aligned parallel to the foliation  
201 plane (Fig. 4d). Opaque minerals are euhedral to subhedral in shape with sizes up to 300  
202  $\mu\text{m}$  and are usually associated with Fe-Mg silicates with which they are aligned (Fig. 4e).  
203 They also occur as inclusions within the biotite and riebeckite. Regarding the leucogranite,  
204 in addition to its modal composition more enriched in quartz and feldspars, it is distinct  
205 with respect to the aegirine-riebeckite granite due to the almost complete absence of Fe-  
206 Mg silicates and the higher abundance of large opaque minerals (Fig. 4f).

207

#### 208 **4. Sampling, materials and analytical procedures**

##### 209 **4.1. Sampling and magnetic measurements**

210 AMS data were based on samples from 25 sites distributed in the Balda granitic massif (Fig.  
211 5a). At each sampling site, two oriented cores were collected using a portable gasoline drill  
212 and oriented by magnetic compass. At the laboratory each core was cut into two or three  
213 oriented specimens of standard size (22 mm in length x 25mm in diameter). A total of 109  
214 specimens were obtained. AMS analyses were performed in two different laboratories: (i)  
215 65 specimens were measured at Géosciences Environnement Toulouse (GET, France) by  
216 using an AGICO KLY5-A Kappabridge equipped with a rapid 3D-Rotator, and the other 44  
217 specimens were measured at the Laboratório de Paleomagnetismo of the University of São  
218 Paulo (USPmag, Brazil) by using an AGICO MFK1-FA Kappabridge. The anisotropy tensor  
219 ( $K_1 \geq K_2 \geq K_3$ ) reconstruction and statistical analyses at the sample and site levels were  
220 performed using ANISOFT 4.2 software (Chadima and Jelinek, 2009). The working data for  
221 each station are as follows: bulk susceptibility magnitude,  $K_m = (K_1 + K_2 + K_3)/3$  ; magnetic  
222 lineation,  $K_1$ ; pole of magnetic foliation plane,  $K_3$  ; anisotropy percentage,  $P\% = [((K_1/K_3) -$   
223  $1) \times 100]$ ; Jelinek (1981) shape parameter, (T), expressed by  $T = [\ln(K_2/K_3) - \ln(K_1/K_3)] /$   
224  $[\ln(K_2/K_3) + \ln(K_1/K_2)]$  ; planar anisotropy,  $F = K_2/K_3$  ; linear anisotropy,  $L = K_1/K_2$ . To  
225 investigate the rock magnetic mineralogy, thermomagnetic experiments were performed  
226 on three selected representative samples: BA7 ( $K_m = 0.9 \times 10^{-3}$  SI), BA16 ( $K_m = 11.5 \times 10^{-3}$  SI),  
227 and BA18 ( $K_m = 3.9 \times 10^{-3}$  SI) at Géosciences Montpellier (GM, France) by using a CS-2  
228 furnace coupled with an AGICO KLY3 Kappabridge. In addition, microstructural analysis was  
229 performed to complement the AMS study and determine the kinematics of deformation.  
230 This was performed on oriented thin sections prepared parallel to the  $K_1$ - $K_3$  plane of the  
231 AMS ellipsoid of the granite samples. Samples were selected based on their geographical  
232 distribution within the pluton and the presence or absence of mesoscopic fabrics. Thus, 9

233 thin sections from granites with mesoscopic fabrics and 5 from granites without  
234 mesoscopic fabrics were analyzed.

235

#### 236 **4.2. U-Pb zircon dating**

237 Sample preparation and analyses were performed at the Géosciences Environnement  
238 Toulouse laboratory (GET, France). After crushing and sieving the rock samples, ~3 kg of  
239 powder was manually washed in a plastic gold pan to remove the clays and to concentrate  
240 the heavy minerals. Following this step, zircons were directly handpicked under a binocular  
241 microscope without any criterion of selection, set in epoxy mounts, and polished down to a  
242 sub-equatorial section. The internal structures of the grains were documented by a  
243 cathodoluminescence (CL) imaging using a Tescan Vega scanning electron microscope  
244 (SEM) equipped with a panchromatic CL detector at GET (10 kV voltage, 3 nA beam  
245 current).

246 Analyses of U-Pb isotopes and trace elements in zircon were simultaneously performed by  
247 laser ablation-inductively coupled plasma-mass spectrometry (LA-ICP-MS) from the same  
248 ablation craters. The analyses were carried out at the Service ICP-MS of Observatoire Midi-  
249 Pyrénées (OMP-UMS831) at GET, using an NWR femto (Elemental Scientific Instruments)  
250 solid-state (257 nm) femtosecond laser ablation system (pulse duration ca. 235 fs) coupled  
251 to an Element XR (Thermo) sector-field ICP-MS. A laser repetition rate of 7 Hz, a spot  
252 diameter of 30  $\mu\text{m}$  and a laser fluence of ca.  $2.4 \text{ J}\cdot\text{cm}^{-2}$  were employed. The sample surface  
253 was cleaned immediately before each analysis, using four pre-ablation pulses. Ablation was  
254 performed in a built-in, dual-volume, fast-washout ablation cell ( $<1 \text{ cm}^3$  effective volume)  
255 fluxed with carrier gas consisting of ca.  $0.6 \text{ L}\cdot\text{min}^{-1}$  He. Make-up gas, consisting of ca. 0.88

256 L.min<sup>-1</sup> Ar was admixed downstream of the ablation cell. Each analysis consisted in 20 s of  
257 background acquisition followed by 25 s of sample ablation. The ICP-MS instrument was  
258 optimized for maximum sensitivity on Th and U while keeping low the production of oxides  
259 (<sup>254</sup>UO<sup>+</sup>/<sup>238</sup>U<sup>+</sup> ≤0.1%) and the Th/U ratio as close to 1 as possible (on NIST SRM610 glass). A  
260 list of acquired masses and corresponding dwell times is provided in Supplementary Table  
261 1.

262 The resulting intensities were processed offline using the Igor Pro Iolite v2.5  
263 software (Hellstrom et al., 2008), the VizualAge data reduction scheme (Petrus and  
264 Kamber, 2012) for U-Pb dating, and the built-in data reduction scheme for trace elements.  
265 Background-subtracted intensities were used to calculate isotope ratios, which were  
266 corrected for laser-induced Pb/U fractionation (Paton et al., 2010), mass discrimination,  
267 and drift during the analytical session by conventional standard-sample bracketing against  
268 zircon reference material GJ-1 (Jackson et al., 2004 using isotope ratios recommended by  
269 Horstwood et al., 2016). No common Pb corrections were performed. Data from secondary  
270 zircon reference materials AUSZ7-1 (Kennedy et al., 2014), Plešovice (Sláma et al., 2008)  
271 and 91500 (Wiedenbeck et al., 1995) were processed as unknown to check the accuracy of  
272 the corrections. The obtained ages for all secondary standards were accurate within less  
273 than 1% relative (see Supplementary Table 1). Systematic uncertainties were propagated in  
274 the uncertainties of calculated dates following the procedure of Horstwood et al. (2016)  
275 (see details in Supplementary Table 1). Trace element concentrations were calibrated  
276 against the NIST SRM610 glass reference material (Jochum et al., 2011) using the  
277 stoichiometric Si content of zircon (15 wt. %) as internal standard for relative sensitivity  
278 correction and the same signal integration intervals as defined for U-Pb dating. The  
279 accuracy of the obtained Ti concentrations was ensured by normalization to the ID-TIMS

280 determined concentration of the 91500 zircon reference material (Szymanowski et al.,  
281 2018). More details about the analytical conditions, as well as the data from zircon in the  
282 investigated Balda granite sample and secondary reference materials, are provided in  
283 Supplementary Table 1.

284

## 285 **5. Results**

### 286 **5.1. Magnetic data**

#### 287 **5.1.1. Scalar data**

288 The range of bulk volume magnetic susceptibility ( $K_m$ ) values for the analyzed stations  
289 spans from  $0.19 \times 10^{-3}$  to  $21.98 \times 10^{-3}$  SI (Table 1), with a mean value of  $5.68 \times 10^{-3}$  SI and a  
290 standard deviation of  $6.91 \times 10^{-3}$  SI. This variability reflects the diversity of magnetic  
291 mineralogy, which in turn controls the Anisotropy of Magnetic Susceptibility (AMS).  
292 Notably, 8% of the sites exhibited low  $K_m$  ( $<0.5 \times 10^{-3}$  SI), indicative of a dominant  
293 paramagnetic mineral assemblage (Rochette, 1987; Bouchez, 1997). On the other hand,  
294 56% of the sites displayed intermediate  $K_m$  ( $0.5 \times 10^{-3} < K_m < 5 \times 10^{-3}$  SI), suggesting a  
295 combined influence of paramagnetic and ferromagnetic minerals (Bouchez, 2000;  
296 Borradaile, 2001; Hrouda, 2007) or the presence of hematite derived from martitization of  
297 magnetite grains (Sant'Ovaia et al., 2024). Lastly, 36% of the sites showed a high  $K_m$  ( $>5 \times$   
298  $10^{-3}$  SI), which is characteristic of ferromagnetic mineral dominance (Hrouda, 2007).

299 In the map view (Fig. 5b) the highest  $K_m$  values were mainly located toward the  
300 northeastern end of the massif, where the leucogranite facies crops out. This is consistent  
301 with the petrographic examination of thin sections that reveals the abundant occurrence of  
302 opaque minerals (Fig. 4f), probably magnetite, within these leucogranites.

303 The anisotropy degree (P %) values vary from 2.8 to 58.7 %, with a mean of 15 %, which is  
304 higher than those commonly observed in granitoids (Bouchez, 1997). The P% vs. Km  
305 diagram (Fig. 6a) shows a roughly positive correlation. This suggests that the P% values may  
306 be related to the abundance and distribution of magnetite grains in the rocks. However,  
307 there are sites with higher P% values than those with much higher Km values (e.g.: BA14,  
308 BA19, BA27). When the P% values are reported in the map (Fig. 7a), we found the greatest  
309 anisotropies (P % > 10) toward the pluton borders, while lower anisotropies (P % < 7) were  
310 dominant at the inner portion of the intrusion, where the field foliation was generally less  
311 pronounced or non-visible. This suggests that the inner part of the granitic body was less  
312 affected by regional deformation.

313 The shape parameter (T) values range from -0.78 to 0.48, indicating that the magnetic  
314 ellipsoid shapes varied from prolate to oblate (Fig. 6b). Oblate magnetic fabrics (T > 0)  
315 account for 68 % of the specimens. The dominant oblate ellipsoids are indicative of a  
316 flattening strain, in agreement with the absence of macroscopic lineation. This dominant  
317 flattening likely originated from the shape of the magnetite grain fabric in the  
318 ferromagnetic samples. In samples with mixed para/ferromagnetic fabrics, biotite may also  
319 contribute significantly to flattening strain. In the map view (Fig. 7b), the oblate ellipsoids  
320 mainly occupied the northeast half of the pluton, where the body was less thick, whereas  
321 the prolate ellipsoids (T > 0) were restricted to the aegirine-riebeckite granite facies (SW).

### 322 **5.1.2. Directional data**

323 The statistical significance of the magnetic lineation and foliation per site was  
324 expressed by the values of Jelinek's elliptical confidence angles E12 and E31 (Jelinek 1978),  
325 respectively. According to several studies (Archanjo and Fetter, 2004; Pueyo et al., 2004; Li

326 et al., 2019), these values were found to be reliable when they were lower than 25°. For  
327 the Balda pluton, only two sites (#13, #14) show an E12 higher than 25° (Table 1). However,  
328 the magnetic fabrics of these sites are concordant with those of the surrounding sites.  
329 Therefore, these two sites were also considered in this study. The magnetic foliation is  
330 roughly parallel to the field foliation and dips steeply from NNE to NE or from SSW to SW.  
331 The mean strike/dip of the (K1K2) plane is 33°E/80°WNW (Fig. 8a). The magnetic lineations  
332 are shallowly plunging (<35°) from SSW to SW (mean trend/plunge is 214°/16°; Fig. 8b). It is  
333 noteworthy that, globally, the strike of the magnetic foliation and lineation are regular and  
334 sub-parallel to the pluton NNE-SSW long axis, except for station #27.

### 335 **5.1.3. Magnetic mineralogy**

336 Reflected light microscopic examinations suggest the presence of magnetite grains in all  
337 studied thin sections. The Km values of the Balda granite indicate a ferromagnetic  
338 mineralogy, where magnetite dominates the iron-bearing silicates in both susceptibility  
339 and anisotropy, in 36% of the samples. In 56% of the samples, a mixed para-/ferromagnetic  
340 mineralogy is observed, characterized by the coexistence of ferromagnetic and  
341 paramagnetic minerals without any single species dominating. To further investigate this  
342 magnetic mineralogy, thermomagnetic measurements were conducted on ferromagnetic  
343 sample BA18 ( $Km=11.5 \times 10^{-3}$  SI), as well as on the para-/ferromagnetic samples BA16  
344 ( $Km=3.9 \times 10^{-3}$  SI) and BA7 ( $Km=0.9 \times 10^{-3}$  SI). All these samples exhibit an abrupt drop in  
345 magnetic susceptibility at approximately 580°C (Fig. 9), indicative of magnetite phases.  
346 However, for the samples BA16 and BA18 (Fig. 9a and 9b), the heating and cooling curves  
347 are reversible, suggesting that the magnetic minerals are generally stable and do not  
348 undergo transformation during the experiment. In contrast, the mixed para-/ferromagnetic

349 sample BA7 (Fig. 9c) shows a heating curve with lower susceptibility than the cooling curve,  
350 indicating significant neoformation of ferromagnetic minerals during the heating cycle.  
351 Additionally, the K–T curves for this sample exhibit a Hopkinson peak below the Curie  
352 point, revealing the small sizes of the magnetite grains in this mixed para-/ferromagnetic  
353 sample (Dunlop, 2014).

## 354 **5.2. Microstructure**

355 Under the microscope, the aegirine-riebeckite granite and leucogranite samples devoid of  
356 macroscopic fabrics reveals the presence of a planar fabric underlined by the preferential  
357 orientation of Fe-Mg silicates and opaque minerals sub-parallel to the foliation (Fig. 4d and  
358 e). These rocks are also characterized by low or no biotite, which contributes their isotropic  
359 macroscopic appearance in some places (Flood, 1988). According to microstructural criteria  
360 (Passchier and Trouw, 2005; Nédélec and Bouchez, 2015), all the studied granite samples of  
361 the Balda pluton display high-temperature solid-state microstructures, as shown by quartz  
362 grains with strong undulose extinction and ubiquity of recrystallized quartz grains. These  
363 recrystallized grains show little or no intragranular deformation and are often polygonal in  
364 shape with  $120^\circ$  triple points (Fig. 10a) indicating that high temperatures have been  
365 maintained long enough after the end of deformation (Bons and Urai, 1992; Passchier and  
366 Trouw, 2005). These rocks are devoid of submagmatic microstructures (evidence for crystal  
367 deformation and the contemporaneous presence of melt).

368 Deformation of the granite is marked by monocrystalline quartz ribbons and  
369 microstructural assemblages typical of dynamic recrystallization dominated by grain  
370 boundary migration (GBM) and sub-grain rotation (SGR) processes. The GBM is highlighted  
371 by interfingering quartz-quartz boundaries (Fig. 10b) and lobate quartz and feldspar

372 boundaries (Fig. 10c), while SGR is typified by aggregates of recrystallized quartz grains  
373 elongate (Fig. 10d), occasionally associated with biotite lamella, wrapped around larger  
374 elongated feldspar or elongate quartz grains with a preferred orientation that defines a  
375 continuous foliation and shear bands or C-planes (Fig. 10e) that suggests gneissification  
376 (Bouchez and Nicolas, 2021). This trend is particularly accentuated in samples collected  
377 from the pluton margins (e.g., sites BA11, BA25), corroborating the interpretation of more  
378 intense deformation at the periphery compared to the core, as suggested by both field  
379 observations and AMS data.

380 In several thin sections prepared parallel to the subhorizontal magnetic lineation and  
381 perpendicular to the magnetic foliation, several microstructures all point to sinistral sense  
382 of shear, including porphyroclast systems; fish-shaped riebeckite; and grain aggregates,  
383 formed by dynamic recrystallization of feldspars and quartz, with monoclinic symmetry  
384 (Fig. 10e to h).

385

### 386 **5.3. U-Pb dating on zircon and chemical composition**

387 Zircon grains dated in this study come from an aegirine-riebeckite granite sampled at the  
388 southeast border of the Balda massif (Station #16). The sample PA01 is homogeneous,  
389 heterogranular and grey in color. In thin section, the sample displays microstructures  
390 indicative of solid-state deformation at high temperatures. The zircon crystals are usually  
391 transparent and light yellow in color, euhedral, 320-130  $\mu\text{m}$  long and 200-70  $\mu\text{m}$  wide, with  
392 length/width ratios ranging from 5:3 to 2:1. The textures of the zircon grains investigated in  
393 CL images allow to clearly distinguish two generations: (i) numerous zircon crystals are  
394 characterized by bright luminescence and oscillatory to sector zoning with, for some of  
395 them, a featureless and CL-dark rim up to  $\square 30 \mu\text{m}$  thick; and (ii) some crystals showing

396 dark luminescence, lacking oscillatory zoning (in that sense, they resemble the dark rims  
397 around bright-CL crystals) and a "dirty" aspect, i.e. cluttered with numerous tiny inclusions  
398 and pores (Supplementary Fig. 1). In the following, we refer to these two generations as  
399 "bright" and "dark" zircons respectively.

400 A total of 58 spots were analyzed on 44 zircon grains (Table 2). "Bright" zircons (42 spots)  
401 exhibited Th/U ratios ranging from 0.1 to 0.6 (average = 0.4), whereas "dark" zircons (13  
402 spots) and dark rims of "bright" zircons (3 spots, incorporated into the "dark" group)  
403 displayed Th/U ratios between 0.2 and 2.8 (average = 1.2). These values align with  
404 expected ranges for magmatic zircons (Hoskin & Black, 2000). However, significant  
405 differences were observed in the chemical compositions of the two zircon generations (Fig.  
406 11; Table 3). "Dark" zircons displayed consistently wider ranges and higher average  
407 contents of Th (152-7100 ppm, average = 2241 ppm), U (336-3100 ppm, average = 1500  
408 ppm), Ti (18-10500 ppm, average = 872 ppm), Hf (8980-18750 ppm, average = 14397 ppm),  
409 and total REE (1586-22251 ppm, average = 120000 ppm) compared to "bright" zircons (Th:  
410 23-225 ppm, average = 79 ppm; U: 59-611 ppm, average = 187 ppm; Ti: 2.8-440 ppm,  
411 average = 21 ppm; Hf: 6720-12580 ppm, average = 8506 ppm; total REE: 1059-6454 ppm,  
412 average = 3284 ppm). Both "bright" and "dark" zircons exhibited negative Eu anomalies.  
413 However, "bright" zircons displayed chondrite-normalized REE patterns characterized by  
414 positive Ce and Sm anomalies alongside a negative Pr anomaly (Fig. 11c). Low  $(La/Yb)_N$   
415 ratios (0.00002-0.156, average = 0.011) further confirm LREE depletion relative to HREE in  
416 "bright" zircons. On the Tera-Wasserburg concordia diagram, many data points are  
417 discordant and define a broad trend pointing towards the Pb isotopic composition of initial  
418 Pb. No statistically robust linear discordia array can be defined from the 59 analyses  
419 considered together (Fig. 12a). However, when considering separately data from "bright"

420 zircons and "dark" zircons, each population yields more robust lower intercept dates of  
421  $729.9 \pm 3.5$  |  $7.5$  Ma (MSWD = 0.89, n = 42; without | with systematic uncertainty  
422 propagation) and  $677.6 \pm 18.9$  |  $19.9$  Ma (MSWD = 2.1, n = 17; without | with systematic  
423 uncertainty propagation), respectively (Fig. 12b&c). In addition, for "bright" zircons, twenty  
424 points are concordant and yield a Concordia date of  $732.7 \pm 3.5$  |  $7.5$  Ma (MSWD<sub>C+E</sub> = 0.62,  
425 n = 20; without | with systematic uncertainty propagation) (Fig. 12d), identical within  
426 uncertainty to the lower intercept date.

## 427 **6. Discussion**

### 428 **6.1. Interpretation of zircon U-Pb data**

429 The zircon textures and U-Pb data obtained from the investigated Balda granite sample  
430 reveal the existence of two zircon generations, namely a group of "bright" grains  
431 crystallized at ca. 730 Ma and "dark" grains yielding a lower intercept date of ca. 680 Ma  
432 (see section 5.3 and Fig. 12). This observation could be interpreted in two different ways:  
433 (i) The ca. 730 Ma "bright" zircons correspond to igneous zircon crystallized during the  
434 emplacement of the Balda granite, and the ca. 680 Ma "dark" rims and grains correspond  
435 to zircon (re-)crystallized during a younger tectono-metamorphic or alteration event; (ii)  
436 The magmatic zircons are represented by the ca. 680 Ma "dark" rims and grains and the ca.  
437 730 Ma "bright" zircons represent xenocrystic and/or inherited zircon from the protolith.

438 We favor the first interpretation for several reasons. First, texturally, the "bright"  
439 zircons represent a homogeneous population showing typically igneous, oscillatory or  
440 sector zoning. These grains lack any clear resorption or dissolution feature, as would be  
441 expected from xenocrystic or inherited zircon (e.g., Vavra et al., 1999; Corfu et al., 2003;  
442 Laurent et al., 2017, 2023). Second, the relatively high Zr solubility in alkaline melts  
443 compared to other (peraluminous or metaluminous) silicic melts (Gervasoni et al., 2016; Shao

444 et al., 2020; Crisp and Berry, 2022) makes the complete survival of xenocrystic or inherited  
445 zircon very unlikely in a former alkaline magma like the Balda granite. Lastly, the two zircon  
446 generations show distinct trace element signatures, with the “bright” cores and grains  
447 exhibiting clearly igneous compositions (relatively low Th and U contents (Fig. 11a), steep  
448 REE patterns with very low  $La_N/Yb_N$ , positive Ce and negative Eu anomalies (Fig. 11c)  
449 whereas the “dark” rims and grains have chemical affinities with metamorphic or altered  
450 zircon (high LREE, Ti, Y, Th and U contents) (e.g. Corfu et al., 2003; Hoskin, 2005; Grimes et  
451 al., 2009; Bell et al., 2016).

452 Therefore, we interpret the “bright” zircons as igneous crystals, such that their  
453 Concordia date of  $732.7 \pm 7.5$  Ma is considered as the emplacement and crystallization age  
454 of the Balda granite. The “dark” rims and grains would correspond to zircon growth or  
455 recrystallization during a late, alteration or metamorphic event that occurred at  $677.6 \pm$   
456  $19.9$  Ma. The significance of this age interpretation for the regional and general geological  
457 context is further developed in section 6.3 below.

458

## 459 **6.2 Magnetic susceptibility sources and AMS significance**

460 Magnetic susceptibility ( $K_m$ ) measurements enabled the classification of the Balda  
461 pluton into three distinct magnetic categories. Notably, 8% of the samples exhibited  
462 paramagnetic behavior, while 56% displayed mixed magnetic character. The remaining 36%  
463 were classified as ferromagnetic with  $K_m$  exceeding  $5 \cdot 10^{-3}$  SI. The dominance of the  
464 ferromagnetic character in the latter category suggests that magnetite is the primary  
465 contributor (Hrouda, 2007). In addition, thin-section observations reveal the presence of  
466 large euhedral to subhedral opaque minerals. Thermomagnetic analysis confirmed that the  
467 ferromagnetic minerals in these samples were primarily magnetite. Nédélec and Bouchez

468 (2015) demonstrated a strong correlation between the magnetic fabric of magnetite grains  
469 and the overall petrofabric of ferromagnetic granites. Our microstructural observations  
470 were consistent with this finding, as the foliation defined by the alignment of Fe-Mg  
471 silicates coincides with the shape-preferred orientation of magnetite grains within the rock.  
472 The majority of the analyzed sites displayed mixed magnetic mineralogy, characterized by  
473 the coexistence of minor magnetite with paramagnetic minerals (biotite, aegirine, and  
474 riebeckite). This combination results in a composite magnetic fabric that reflects the  
475 combined influence of both the ferromagnetic and paramagnetic components. According  
476 to Bouchez (2000), the magnetic fabrics in these mineral classes have contrasting origins.  
477 The fabric of ferromagnetic minerals, primarily magnetite, reflects their preferred  
478 orientation within the rock. In contrast, the fabric of paramagnetic minerals is governed by  
479 their inherent magnetocrystalline anisotropies. Notably, in the absence of cordierite and  
480 tourmaline, the principal orientations of the ellipsoids representing the two fabrics tend to  
481 coincide, although their axial ratios may differ (Rochette et al., 1994 ; Nédélec and  
482 Bouchez, 2015). Therefore, the resultant magnetic fabric in the mixed-mineralogy samples  
483 retains a well-defined foliation and lineation, exhibiting minimal variation compared to  
484 purely ferromagnetic sites. This remarkable congruence eliminates the need for separate  
485 analysis, solidifying the argument that the AMS measurements obtained can be considered  
486 as reliable markers of the Balda-granite petrofabric.

### 487 **6.3. Time relationship between emplacement and global tectonics**

488 Pluton emplacement relative to regional deformation is fundamental to the  
489 reconstruction of the poorly-constrained geodynamic evolution of the Central African  
490 Orogenic Belt. According to the U-Pb zircon dating results and interpretation, the Balda  
491 granite was emplaced at  $732.7 \pm 7.5$  Ma, i.e., prior to the Pan-African regional deformation

492 that starts at  $668 \pm 11$  Ma in the North-West Cameroon domain (Tchameni et al., 2016).  
493 This new U-Pb age highlights the emplacement of a pre-orogenic Sturtian magmatism in  
494 the area. The pre-tectonic emplacement of the Balda granite is also supported by regional  
495 tectono-chronological evidence. Indeed, previous studies (Penaye et al., 2006; Isseini et al.,  
496 2012; Dawai et al., 2013; Tchameni et al., 2016; Bouyo Houketchang et al., 2016; Toteu et  
497 al., 2022) have shown that plutonism in the neighboring areas in north Cameroon and in  
498 southeast Chad started as early as 750 Ma. Within the Central African Orogenic Belt, the  
499 emplacement of syn- to late- tectonic intrusions is restricted between 670 and 580 Ma  
500 during the Ediacaran (Dawai et al., 2013; Tchameni et al., 2016; Basua et al., 2022; Isseini et  
501 al., 2012; Nomo Negue et al., 2017). The age of  $677.6 \pm 19.9$  Ma obtained on the “dark”  
502 zircon rims is consistent with this timeline, insofar it overlaps with the inferred onset of  
503 Pan-African deformation in the area ( $668 \pm 11$  Ma; Tchameni et al., 2016). This age possibly  
504 directly dates the deformation of the Balda pluton.

505 Our AMS investigations show that the magnetic foliation and lineation are  
506 consistently oriented throughout the pluton: foliation has NNE to NE strikes and dip  
507 steeply, and lineation plunges gently to the SSW or SW. Furthermore, these magnetic  
508 fabrics were parallel to the elongation axis of the pluton. This, combined with the sense of  
509 shear observed in thin sections, suggests that the Balda granite fabrics have been  
510 controlled by a local sinistral shear zone that marks the regional deformation. The origin of  
511 the Balda fabric is associated with the intense Pan-African deformation and can be  
512 considered as a metamorphic fabric. Unfortunately, in the case of the Balda pluton, the  
513 host rocks are not observable because of the Quaternary sedimentary deposits that  
514 completely cover them. Therefore, only the pre-orogenic Balda pluton can be used as  
515 regional indicator. Alternatively, we compared the internal structure of the pluton with

516 that of the potential host rocks at the regional scale. According to the geological map of the  
517 Northern Cameroon and South-West Chad regions (Penaye et al., 2006; Fig. 1) the granitic  
518 pluton of Balda is located within the northward extension of the Mayo-Kébbi domain.  
519 Considering this configuration, the Poli-Léré-Maroua greenstone belt group (800-700 Ma;  
520 Penaye et al., 2006; Doumnang, 2006; Isseini, 2011) appears to be the most probable host  
521 rock unit for the Balda granite. Mesoscopic  $S_2$  foliation of the regional deformation  $D_2$  in  
522 this greenstone belt group is predominantly subvertical and orientated NNE-SSW (Poucllet  
523 et al., 2006; Isseini, 2011), similar in strike and dip to magnetic foliation in the Balda pluton  
524 (best pole: 127/4) as well as to the  $S_2$  foliation (best pole: 297/4) recorded in different  
525 lithological units of the far North Cameroon area (Dumort and Peronne, 1966; Fig. 8).

526 At first glance, this foliation similarity would corroborate the pre-tectonic  
527 emplacement of the Balda granite with respect to regional  $D_2$ . This is supported by the  
528 absence of magmatic or submagmatic fabrics in the Balda pluton, its orthogneissic aspect  
529 and, more importantly, the pre-tectonic nature suggested by porphyroclasts and sigmoidals  
530 that resulted from post-emplacement strain. As evidenced in several studies (Aranguren et  
531 al., 1996; Tomezzoli et al., 2003; Tripathi et al., 2012), the AMS of granitic rocks is usually  
532 modified during gneissification and often records the latest incremental deformation that  
533 has affected the granite. Benn (1994) also demonstrated through numerical modeling that  
534 the magnetic fabric of granite can be modified by even a small amount of post-  
535 emplacement strain. This post-emplacement deformation is corroborated by the dominant  
536 high  $P\%$  values (up to 58 %) recorded for the Balda pluton. Indeed, solid-state deformation  
537 generally leads to a strong geometric organization of grains and, therefore, to strong  
538 distribution anisotropy (Nédélec and Bouchez, 2015).

539

#### 540 **6.4. Deformation regime**

541 The homogeneous NNE-trending subvertical foliation and subhorizontal lineation  
542 recognized by the AMS in the Balda pluton, as well as the parallelism of these structures  
543 with the pluton elongation, approximates a simple shear deformation in relation to the  
544 transcurrent shear zone. However, the occurrence of markedly more oblate (68%) than  
545 prolate (32%) magnetic fabric suggests the role of a simultaneous component of flattening  
546 denoting a transpressional deformation regime, that is, a strike-slip deformation that  
547 deviates from simple shear with a combination of shortening orthogonal to the  
548 deformation zone (Sanderson and Marchini, 1984; Tikoff and Teyssier, 1994). Several  
549 studies have shown that AMS ellipsoids ( $K_1 > K_2 > K_3$ ) of deformed rocks are (sub) parallel to  
550 the principal axes of the strain ellipsoid ( $X > Y > Z$ ), and that the  $K_1$  axis is analogous to the  
551 stretching lineation (e.g., Burmeister et al., 2009; Mamtani and Vishnu, 2012; Ferré et al.,  
552 2014; Parsons et al., 2016; Mamtani et al., 2017; Goswami et al., 2018). According to the  
553 model of Fossen and Tikoff (1993), vertical foliation combined with subhorizontal  
554 stretching lineation, as recorded in the Balda pluton, is indicative of a transpression regime  
555 dominated by simple shear. Therefore, deformation in the Balda area is consistent with a  
556 sinistral wrench-dominated transpressional setting as we can observe in other syn-tectonic  
557 intrusions in Cameroon (Ngako et al., 2008; Nsifa et al., 2013; Fozing et al., 2016).

#### 558 **6.5. Geodynamic significance**

559 The geochronological results have revealed that the emplacement of the Balda alkaline  
560 granite dates from  $732.7 \pm 7.5$  Ma. This Sturtian age is significantly older than, but broadly  
561 corresponds to the same, early igneous event as that of the Djabé alkaline granite ( $707.7 \pm$   
562  $2.5$  Ma; Basua et al., 2022) located approximately 150 km to the SSW. Although the latter

563 has not been the subject of detailed structural studies, it has also been described as a  
564 deformed alkaline granite (Basua et al., 2022). These two plutons are localized along the  
565 border between the NW Cameroon and Mayo-Kebbi domains. Therefore, these alkaline  
566 granites appear to be relevant markers of the regional geodynamic evolution. Alkaline  
567 granite deformation can be related to syn- tectonic regimes (compression/transpression)  
568 (Nsifa et al., 2013; Valentin et al., 2020) or collisional tectonics later to their emplacement  
569 (Ashwal et al. 2007; Nanda et al. 2009; Ranjan et al., 2018). Burke et al. (2003) qualify the  
570 latter as “deformed alkaline rocks with or without carbonatites” (DARCs). As previously  
571 demonstrated, the Balda pluton is characteristically deformed subsequently to its  
572 emplacement. Therefore, it possibly corresponds to a DARC. The two main hypotheses  
573 proposed for the origins of DARCs situated near terrane boundaries are that they may be  
574 remnants of ancient suture zones formed during the early Wilson cycle or relics of syn-  
575 orogenic extension (back-arc basins) that underwent tectonization during collisional  
576 orogeny. According to the findings of previous studies and the present investigation, there  
577 is strong evidence of continental tholeiitic magmatism, characterized by the intrusion of  
578 gabbro-norites that date back to  $737 \pm 1$  Ma (Penaye et al., 2006; Pouclet et al., 2006).  
579 Additionally, the presence of alkaline magmatism, such as the Balda granite ( $732.7 \pm 3.5$   
580 Ma) and the Djabé granite ( $707.7 \pm 2.5$  Ma; Basua et al., 2022), reinforces the hypothesis of  
581 an association with a continental extensional setting. The question of whether this  
582 continental extension marks the beginning of the Wilson cycle or corresponds to a syn-  
583 orogenic extension remains open. However, the hypothesis of syn-orogenic extension  
584 seems plausible and consistent with regional data. These two points support our  
585 hypothesis.

586 (1) Notably, the time interval between the emplacement of the Balda granite ( $\approx 732$   
587 Ma) and the CAOB collisional phase ( $\approx 690$  Ma) is significantly shorter (40-50 million years)  
588 than the typical duration of the Wilson cycle ( $>400$ -600 Ma).

589 (2) The greenstone belt rocks of the Poli-Léré-Maroua series, hosting the  
590 gabbro-norites, Djabé alkaline granite, and potentially the Balda pluton, were emplaced  
591 between 800 and 790 Ma and display a magmatic arc geochemical signature (Pouclet et al.,  
592 2006). This signature, which is characteristic of subduction zones indicates their formation  
593 in a subduction-related geodynamic environment.

594 These observations call for a syn-orogenic extension in a back-arc basin environment (Fig.  
595 13).

## 596 **7. Conclusion**

597 The present study, combining field observations, microscopic observations, AMS, and  
598 zircon U-Pb geochronology, led to the following conclusions.

599 The Balda pluton consists of deformed alkaline granitic rocks, whose mineralogical  
600 composition includes aegirine and riebeckite, emplaced at  $732.7 \pm 7.5$  Ma within pre-  
601 existing rocks that are now fully covered by alluvial deposits. Magnetic investigations  
602 indicate that these granitic rocks exhibit predominantly ferromagnetic behavior owing to  
603 the presence of magnetite in their mineralogical composition. The microstructures and  
604 zircon geochronology suggest that deformation and AMS development postdated pluton  
605 emplacement. The AMS data, showing subvertical foliation and subhorizontal lineation  
606 fabrics constantly oriented in the NNE-SSW direction, indicate that this deformation was  
607 accommodated by a simple shear-dominated transpression with sinistral kinematics during  
608 the regional Pan-African tectonic, possibly at  $677.6 \pm 19.9$  Ma.

609 The Balda granite, the Djabé granite, and other potentially contemporaneous granites  
610 situated along the boundary of the NW Cameroon and Mayo-Kébbi domains are likely to  
611 have formed during syn-orogenic extension. This interpretation, when considered  
612 alongside the results of previous research, suggests that the emplacement of the Balda  
613 granite might be linked to the formation of a back-arc basin that arose due to the closure  
614 of a paleo-ocean between the NW Cameroon and Mayo-Kébbi domains. However, it is  
615 suggested that exploratory studies be conducted on Tonian formations within this  
616 proposed framework to further substantiate this hypothesis.

### 617 **Acknowledgements**

618 This manuscript is a part of the Ph.D. work of the first author. These research endeavors  
619 received financial support from the University of Maroua through the "Support for Trainer Training  
620 program" granted to the second author, as well as from the CNRS (France) through the LithoCOAC  
621 research project. We would like to express our deep gratitude to Fabienne Barrère de Parseval for  
622 her meticulous preparation of thin sections, Phillipe Olivier for conducting AMS analyses on the first  
623 batch of samples as well as Aurélie Marquet and Françoise Maubé for assistance during LA-ICP-MS  
624 and SEM sessions respectively. We would specially like to thank the Traditional Chief of the Balda  
625 locality for his warm hospitality and its agreement, and Ahmed Blama for his invaluable  
626 contributions in the field. Finally, we express our deep gratitude to the Editor-in-Chief, Prof. Victoria  
627 Pease, Cláudia Cruz, and the anonymous reviewer for their rigorous evaluation process. Their  
628 detailed and pertinent observations have significantly contributed to the improvement in the  
629 quality of this work.

### 630 **References**

631 Abdelsalam, M., G., Liégeois J. P., Stern, R. J., 2002. The Saharan Metacraton. *Journal of*  
632 *African Earth Sciences* 34, 119-136.

633 Aranguren, A., Cuevas, J., Tubía J. M., 1996. Composite magnetic fabrics from S-C  
634 mylonites. *Journal of Structural Geology* 18, (7) 863-869.

635 Archanjo, C. J., and Bouchez, J. L., 1997. Magnetic fabrics and microstructures of the post-  
636 collisional aegirine-augite syenite Triunfo pluton, northeast Brazil. *Journal of Structural*  
637 *Geology* 19(6), 849-860.

638 Archanjo, C. J., Fetter, A. H., 2004. Emplacement setting of the granite sheeted pluton of  
639 Esperanca (Brasiliano orogen, Northeastern Brazil). *Precambrian Research* 135, 193-  
640 215.

641 Arthaud M. H., Caby R., Fuck R.A., Dantas E.L., Parente C.V., 2008. Geology of the northern  
642 Borborema Province, NE Brazil and its correlation with Nigeria, NW Africa. In:  
643 Pankhurst R.J., Trouw R.A.J., Brito Neves B.B., de Wit, M.J. (Eds.). *West Gondwana: Pre-*  
644 *Cenozoic Correlations Across the South Atlantic Region*. London, Geological Society,  
645 *Special Publications* 294(1), 49-67.

646 Ashwal, L.D., Armstrong, R.A., Roberts, R.J., Schmitz, M.D., Corfu, F., Hetherington, C.J.,  
647 Burke, K., Gerber, M., 2007. Geochronology of zircon megacrysts from nepheline  
648 bearing gneisses as constraints on tectonic setting: implications for resetting of the U-  
649 Pb and Lu-Hf isotopic systems. *Contributions to Mineralogy and Petrology* 153, 389-  
650 403

651 Attoh, K., Corfu, F., Nadeau, P.M., 2007. U-Pb zircon age of deformed carbonatite and alkaline  
652 rocks in the Pan-African Dahomeyide suture zone, West Africa. *Precambrian Research*  
653 155, 251-260.

654 Basua, A. A. E., Ma, C., Nguo, K. S., Wang, L. X., Lentz, D. R., Mukherjee, S., Yomeun, B. S.,  
655 2022. Petrogenesis and tectonic setting of A-type granites in the Babouri-Figuil

656 Magmatic Complex (North Cameroon): Constraints from whole rock geochemistry,  
657 zircon U-Pb geochronology and Sr-Nd-Hf isotopes. *Lithos* 414, 106618.

658 Bell, E.A., Boehnke, P., Harrison, T.M., 2016. Recovering the primary geochemistry of Jack  
659 Hills zircons through quantitative estimates of chemical alteration. *Geochimica and*  
660 *Cosmochimica Acta* 191 (C), 187-202.

661 Bella Nké, B.E., Njanko, T., Mamtani, M.A., Njonfang, E., Rochette, P., 2018. Kinematic  
662 evolution of the Mbakop Pan-African granitoids (western Cameroon domain): An  
663 integrated AMS and EBSD approach. *Journal of Structural Geology* 111, 42-63.

664 Benn, K., 1994. Overprinting of magnetic fabrics in granites by small strains: numerical  
665 modelling. *Tectonophysics* 233(3-4), 153-162.

666 Bonin, B., 1990. From orogenic to anorogenic settings: evolution of granitoid suites after a  
667 major orogenesis. *Geological Journal* 25(3-4), 261-270.

668 Bons, P.D., Urai, J.L., 1992. Syn-deformational grain growth: microstructures and kinetics.  
669 *Journal of Structural Geology* 14, 1101-1109.

670 Borradaile, G.J., 2001. Magnetic fabrics and petrofabrics; their orientation distributions and  
671 anisotropies. *Journal of Structural Geology* 23, 1581-1596.

672 Bouchez, J. L., 1997. Granite is never isotropic: an introduction to AMS studies of granitic  
673 rocks. In *Granite: from segregation of melt to emplacement fabrics*. Dordrecht:  
674 Springer Netherlands 95-112.

675 Bouchez, J. L., and Nicolas, A., 2021. *Principles of Rock Deformation and Tectonics*. Oxford  
676 University Press.

677 Bouyo Houketchang, M., Penaye, J., Njel, U.O., Moussango, A.P.I., Sep, J.P.N., Nyama, B.A.,  
678 Wassouo, J.M., Abaté, J.M.E., Yaya, F., Mahamat, A., Hao Ye, Fei Wu, 2016.  
679 Geochronological, geochemical and mineralogical constraints of emplacement depth

680 of TTG suite from the Sinassi Batholith in the Central African Fold Belt (CAFB) of  
681 northern Cameroon: Implications for tectonomagmatic evolution. *Journal of African*  
682 *Earth Sciences* 116, 9-41.

683 Bouyo Houketchang, M., Toteu, S.F., Deloule, E., Penaye, J., Van Schmus, W.R., 2009. U-Pb  
684 and Sm-Nd dating of high-pressure granulites from Tcholliré and Banyo regions:  
685 Evidence for a Pan African granulite facies metamorphism in north-central Cameroon.  
686 *Journal of African Earth Sciences* 54, 144-154.

687 Brito Neves, de B. B., Van Schmus, W. R., Fetter, A., 2002. North-western Africa–North-  
688 eastern Brazil. Major tectonic links and correlation problems. *Journal of African Earth*  
689 *Sciences* 34(3-4), 275-278.

690 Burke, K., and Khan, S., 2006. Geoinformatic approach to global nepheline syenite and  
691 carbonatite distribution: testing a Wilson cycle model. *Geosphere* 2(1), 53-60.

692 Burke, K., Ashwal, L. D., Webb S. J., 2003. New way to map old sutures using deformed  
693 alkaline rocks and carbonatites. *Geology* 31(5), 391- 394.

694 Burke, K., Khan, S. D., Mart, R. W., 2008. Grenville Province and Montereian carbonatite  
695 and nepheline syenite distribution related to rifting, collision, and plume passage.  
696 *Geology* 36(12), 983-986.

697 Burmeister, K.C., Harrinson, M.J., Marshak, S., Ferre, E.C., Bannister, R.A., Kodama, K.P.,  
698 2009. Comparison of Fry strain ellipse and AMS ellipsoid trends to tectonic fabric  
699 trends in very low-strain sandstone of the Appalachian fold-thrust belt. *Journal of*  
700 *Structural Geology* 31(9), 1028-1038.

701 Caby, R., 1989. Precambrian terranes of Benin-Nigeria and northeast Brazil. *Terranes in the*  
702 *circum-Atlantic Paleozoic orogens*, 230, 145.

703 Caxito, F.,A., Santos, L. C. M. L., Ganade C. E., Bendaoud A., Fettous, E. H., Bouyo, M. H.,  
704 2020. Toward an integrated model of geological evolution for NE Brazil-NW Africa: The  
705 Borborema Province and its connections to the Trans-Saharan (Benino-Nigerian and  
706 Tuareg shields) and Central African orogens. *Brazilian Journal of Geology* 50.

707 Chadima, M., and Jelinek, V., 2009. Anisoft 4.2: Anisotropy data browser for windows.  
708 Brno: Advanced Geoscience Instruments Company (AGICO).

709 Corfu, F., Hanchar, J.M., Hoskin, P.W.O., Kinny, P., 2003. Atlas of zircon textures. In  
710 Hanchar, J.M., Hoskin, P.W.O. (eds.): *Zircon. Reviews in Mineralogy* 53, 468-500.

711 Couzinié, S., Ménot, R.P., Doumnang J.C., Paquette, J.L., Rochette, R., Quesnel, R.,  
712 Deschamps, P., Ménot, G., 2020. Crystalline inliers near Lake Iro (SE Chad): Post-  
713 collisional Ediacaran A2-type granitic magmatism at the southern margin of the  
714 Saharan Metacraton. *Journal of African Earth Sciences* 172, 103960.

715 Crisp, L. J., and Berry, A.J. 2022. A new model for zircon saturation in silicate melts.  
716 *Contributions to Mineralogy and Petrology* 177, 71.

717 Dada, S. S., 2008. Proterozoic evolution of the Nigeria-Boborema province. *Geological*  
718 *Society, London, Special Publications* 294(1), 121-136.

719 Dawāï, D., Bouchez, J.L., Paquette, J.L., Tchameni, R., 2013. The Pan-African quartz syenite  
720 of Guider (north-Cameroon): magnetic fabric and U-Pb dating of a late orogenic  
721 emplacement. *Precambrian Research* 236, 132-144.

722 Dawāï, D., Tchameni, R., Bascou, J., Wangmene, S. A., Tchunte, P. M. F., Bouchez, J. L.,  
723 2017. Microstructures and magnetic fabrics of the Ngaoundéré granite pluton  
724 (Cameroon): Implications to the late-Pan-African evolution of Central Cameroon Shear  
725 Zone. *Journal of African Earth Sciences* 129, 887-897.

726 De Wit, M., Stankiewicz, J., Reeves, C., 2008. Restoring Pan-African-Brasiliano connections:  
727 more Gondwana controll, less Tran-Atlantic corruption. Geological Society of London.  
728 Special Publication 294, 399-412.

729 Dilek, Y., and Furnes, H., 2014. Ophiolites and their origins. *Elements* 10(2), 93-100.

730 Djerossem, F., Berger, J., Vanderhaeghe, O., Isseini, M., Ganne, J., Zeh, A., 2020.  
731 Neoproterozoic Magmatic Evolution of the Southern Ouaddaï Massif (Chad). *BSGF -*  
732 *Earth Sciences Bulletin* 191, 34.

733 Doumnang, J. C., 2006. Géologie des formations Néoprotérozoïques du Mayo Kébbi (Sud-  
734 Ouest du Tchad): apport de la pétrologie et de la géochimie: implications sur la  
735 géodynamique au Panafricain (Doctoral dissertation, Orléans).

736 Dumont, J. F., Toteu, S. F., Penaye, J., 1985. Ensembles structuraux et principales phases de  
737 déformations panafricaines dans la zone mobile du Nord Cameroun, région de Poli.  
738 *Revue des Sciences et Techniques, Série Sciences de la Terre, Yaoundé* 1, 9-23.

739 Dumort, J. C., et Peronne, Y., 1966. Notice Explicative sur la Feuille Maroua. 1 Carte  
740 géologique de Reconnaissance au 1/500000. Direction des Mines et de la Géologie,  
741 Yaoundé, Cameroun.

742 Dunlop, D. J., 2014. High-temperature susceptibility of magnetite: a new pseudo-single-  
743 domain effect. *Geophysic Journal International* 199, 707-716.

744 Ferré, E. C., Gébelin, A., Till, J. L., Sassier, C., Burmeister, K. C., 2014. Deformation and  
745 magnetic fabrics in ductile shear zones: a review. *Tectonophysics* 629, 179-188.

746 Ferré, E., Déléris, J., Bouchez, J. L., Lar, A. U., Peucat, J. J., 1996. The Pan-African  
747 reactivation of Eburnean and Archaean provinces in Nigeria: structural and isotopic  
748 data. *Journal of the Geological Society* 153(5), 719-728.

749 Ferré, E., Gleizes, G., Caby, R., 2002. Obliquely convergent tectonics and granite  
750 emplacement in the Trans-Saharan belt of Eastern Nigeria: a synthesis. *Precambrian*  
751 *Research* 114(3-4), 199-219.

752 Flood, R. H., and Vernon, R. H., 1988. Microstructural evidence of orders of crystallization  
753 in granitoid rocks. *Lithos* 21(4), 237-245.

754 Fossen, H., and Tikoff, B., 1993. The deformation matrix for simultaneous simple shearing,  
755 pure shearing and volume change, and its application to transpression-transension  
756 tectonics. *Journal of Structural Geology* 15(3-5), 413-422.

757 Fosso Tchunte, P. M., Tchameni, R., André-Mayer, A. S., Dakoure, H. S., Turlin, F., Poujol,  
758 M., Rouer, O., 2018. Evidence for Nb-Ta occurrences in the syn-tectonic Pan-African  
759 Mayo Salah leucogranite (Northern Cameroon): Constraints from Nb-Ta oxide  
760 mineralogy, geochemistry and U-Pb LA-ICP-MS geochronology on columbite and  
761 monazite. *Minerals* 8(5), 188.

762 Fotso, B. H. K., Nague, E. N., Daouda, D., Fosso Tchunte, P. M., Saha Fouotsa, A. N.,  
763 Tchameni, R., 2022. Petrography and geochemistry of the Letta Pan-African plutonic  
764 and metamorphic rocks in eastern part of the Central African Fold Belt in Cameroon.  
765 *Arabian Journal of Geosciences* 15(20), 1589.

766 Fotso, B. H. K., Nomo, E. N., Dawāi, D., Fosso Tchunte, P. M., Saha Fouotsa, A. N., Tchameni,  
767 R., 2022. Petrography and geochemistry of the Letta Pan-African plutonic and  
768 metamorphic rocks in eastern part of the Central African Fold Belt in  
769 Cameroon. *Arabian Journal of Geosciences* 15(20), 1589.

770 Fozing, E.M., Njanko, T., Seta, N., Kwékam, M., Njonfang E., Rochette P, 2016. Structural  
771 characterization of the Misajé granitic pluton (NW Cameroon): constraints from

772 magnetic and field observations. *International Journal of Earth Sciences* 105, 2285-  
773 2309.

774 Francaise, Direction des Mines et de la Geologie, 24 p.

775 Ganade de Araújo C.E., Cordani U.G., Agbossoumounde Y., Caby R., Basei M.A., Weinberg  
776 R.F., Sato K., 2016. Tightening-up NE Brazil and NW Africa connections: New U–Pb/Lu–  
777 Hf zircon data of a complete plate tectonic cycle in the Dahomey belt of the West  
778 Gondwana Orogen in Togo and Benin. *Precambrian Research* 276, 24-42.

779 Ganade de Araújo C.E., Rubatto D., Hermann J., Cordani U.G., Caby R., Basei M.A.S., 2014.  
780 Ediacaran 2,500-km-long synchronous deep continental subduction in the West  
781 Gondwana Orogen. *Nature Communications*, 5. <https://doi.org/10.1038/ncomms6198>

782 Ganwa, A. A., Klötzli, U. S., Hauzenberger, C., 2016. Evidence for Archean inheritance in the  
783 pre-Pan-African crust of Central Cameroon: insight from zircon internal structure and  
784 LA-MC-ICP-MS UPb ages. *Journal of African Earth Sciences* 120, 12-22.

785 Gervasoni, F., Klemme, S., Rocha-Júnior, E.R.V., Berndt, J., 2016. Zircon saturation in silicate  
786 melts: a new and improved model for aluminous and alkaline melts. *Contributions to*  
787 *Mineralogy and Petrology* 171,429-437.

788 Goswami, S., Mamtani, M. A., Rana, V., 2018. Quartz CPO and kinematic analysis in  
789 deformed rocks devoid of visible stretching lineations: an integrated AMS and EBSD  
790 investigation. *Journal of Structural Geology* 115, 270-283.

791 Grimes, C.B., John, B.E., Cheadle, M.J., Mazdab, F.K., Wooden, J.L., Swapp, S., Schwartz, J.J.,  
792 2009. On the occurrence, trace element geochemistry, and crystallization history of  
793 zircon from in situ ocean lithosphere: *Contributions to Mineralogy and Petrology*. 158,  
794 757-783.

795 Groves, D.I., Santosh M., Goldfarb R.J., Zhang, L., 2018. Structural geometry of orogenic  
796 gold deposits: Implications for exploration of world-class and giant deposits.  
797 *Geosciences Frontiers* 9(14), 1163-1177.

798 Guiraud, M., 1990. Tectono-sedimentary framework of the Early Cretaceous continental  
799 Bima Formation (Upper Benue Trough, N.E. Nigeria). *Journal of African Earth Sciences*,  
800 10, 341-353.

801 Hellstrom J., Paton C., Woodhead, J., Hergt, J., 2008. Lolite: Software for spatially resolved  
802 LA-(quad and MC) ICP-MS analysis, in *Laser ablation ICP-MS in the Earth sciences:*  
803 *Current practices and outstanding issues*, P. Sylvester, Editor. 2008, Mineralogical  
804 Association of Canada: Vancouver, 343-348

805 Horstwood, M. S., Košler, J., Gehrels, G., Jackson, S. E., McLean, N. M., Paton, C., Schoene,  
806 B., 2016. Community-derived standards for LA-ICP-MS U-(Th) Pb geochronology–  
807 Uncertainty propagation, age interpretation and data reporting. *Geostandards and*  
808 *Geoanalytical Research* 40(3), 311-332.

809 Hoskin, P. W. O. and Black, L. P., 2000. Metamorphic zircon formation by solid-state  
810 recrystallization of protolith igneous zircon. *Journal of Metamorphic Geology*, 18(4),  
811 423-439.

812 Hoskin, P.W.O., 2005. Trace-element composition of hydrothermal zircon and the  
813 alteration of Hadean zircon from the Jack Hills, Australia. *Geochimica and*  
814 *Cosmochimica Acta* 69, 637-648.

815 Hrouda, F., 2007. Magnetic susceptibility, anisotropy. In: D. Gubbins and E. Herrero-Bervera  
816 (Eds.), *Encyclopedia of Geomagnetism and Paleomagnetism*. Springer, p.546-560.

817 Hurley, P. M., Rand, J. R., Pinson Jr, W. H., Fairbairn, H. W., de Almeida, F. F. M., Melcher,  
818 G. C., Vandoros, P., 1967. Test of Continental Drift by Comparison of Radiometric Ages:

819 A pre-drift reconstruction shows matching geologic age provinces in West Africa and  
820 Northern Brazil. *Science* 157(3788), 495-500.

821 Isseini, M., 2011. Croissance et différenciation crustales au Néoprotérozoïque: Exemple du  
822 domaine panafricain du Mayo Kébbi au Sud-Ouest du Tchad (Doctoral dissertation,  
823 Université Henri Poincaré-Nancy 1).

824 Isseini, M., André-Mayer, A.S., Vanderhaeghe, O., Barbey, P., Deloule, E., 2012. A type  
825 granite from the Pan-African orogenic belt in south-western Chad constrained using  
826 geochemistry, Sr-Nd isotopes and U-Pb geochronology. *Lithos* 153, 39-52.

827 Jackson, S. E., Pearson, N. J., Griffin, W. L., Belousova, E. A., 2004. The application of laser  
828 ablation-inductively coupled plasma-mass spectrometry to in situ U-Pb zircon  
829 geochronology. *Chemical geology*, 211(1-2), 47-69.

830 Jelínek, V., 1978. Statistical processing of anisotropy of magnetic susceptibility measured  
831 on groups of specimens. *Studia geophysica and geodaetica* 22(1), 50-62.

832 Jelinek, V., 1981. Characterization of the magnetic fabric of rocks. *Tectonophysics* 79(3-4),  
833 T63-T67.

834 Jochum, K. P., Weis, U., Stoll, B., Kuzmin, D., Yang, Q., Raczek, I., Enzweiler, J., 2011.  
835 Determination of reference values for NIST SRM 610-617 glasses following ISO  
836 guidelines. *Geostandards and Geoanalytical Research* 35(4), 397-429.

837 Kasser, M. Y., 1995. Evolution précambrienne de la région du Mayo Kébbi (Tchad). Un  
838 segment de la Chaîne Panafricaine. Unpublished Ph. D. thesis, Muséum d'Histoire  
839 Naturelle de Paris, 1-217.

840 Kasser, M.Y., 1998. Le Précambrien tchadien : l'exemple du Mayo-Kébbi. *Revue scientifique*  
841 du Tchad 5, 51-67

842 Kennedy, A. K., Wotzlaw, J. F., Schaltegger, U., Crowley, J. L., Schmitz, M., 2014. Eocene  
843 zircon reference material for microanalysis of U-Th-Pb isotopes and trace elements.  
844 *The Canadian Mineralogist* 52(3), 409-421.

845 Laurent, O., Couzinié, S., Doucet, L.S., 2023. Timescales of ultra-high temperature  
846 metamorphism and crustal differentiation: Zircon petrochronology from granulite  
847 xenoliths of the Variscan French Massif Central. *Earth and Planetary Science Letters*  
848 611, 118133.

849 Laurent, O., Couzinié, S., Zeh, A., Vanderhaeghe, O., Moyen, J. F., Villaros, A., Gardien, V.,  
850 Chelle-Michou, C., 2017. Protracted, coeval crust and mantle melting during Variscan  
851 late-orogenic evolution: U–Pb dating in the eastern French Massif Central.  
852 *International Journal of African Earth Sciences* 106, 421-451.

853 Leelanandam, C., Burke, K., Ashwal, L. D., Webb, S. J., 2006. Proterozoic mountain building  
854 in Peninsular India: an analysis based primarily on alkaline rock distribution. *Geological*  
855 *Magazine* 143(2), 195-212.

856 Li, Y., Li, S., Liang, W., Lu, R., Zhang, Y., Li, X., Zhang, G., 2019. Incremental emplacement  
857 and syn-tectonic deformation of Late Triassic granites in the Qinling Orogen: Structural  
858 and geochronological constraints. *Gondwana Research* 72, 194-212.

859 Liégeois, J.P, Abdelsalam, M.G., Ennih, N., Ouabadi, A., 2013. Metacraton: nature, genesis  
860 and behavior. *Gondwana Research* 23, 220-237.

861 Liégeois, J.P., Black, R., 1987. Alkaline magmatism subsequent to collision in the Pan-  
862 African belt of the Adrar des Iforas. In: Fitton, J.G., Upton, B.G.J. (Eds.), *Alkaline*  
863 *Igneous Rocks*. Geological Society London 30(1), 381-401. Special Publication 30.

864 Mamtani, M. A., Abhijith, V., Lahiri, S., Rana, V., Bhatt, S., Goswami, S., Renjith, A. R., 2017.  
865 Determining the reference frame for kinematic analysis in S-tectonites using AMS.  
866 Journal of the Geological Society of India 90, 5-8.

867 Mamtani, M. A., and Vishnu, C. S., 2012. Does AMS data from micaceous quartzite provide  
868 information about shape of the strain ellipsoid?. International Journal of Earth Sciences  
869 101, 693-703.

870 Nanda, J., Gupta, S., Mamtani, M.A., 2009. Analysis of deformation fabric in an Alkaline  
871 Complex (Koraput): Implications for time relationship between emplacement, fabric  
872 development and regional tectonics. Journal of Geological Society of India 74, 78-94.

873 Nédélec, A., and Bouchez, J. L, 2015. Granites: Petrology, Structure, Geological setting, and  
874 Metallogeny Oxford University Press. New York, 331 pp.

875 Ngako, F., Jegouzo, P., Nzenti, J. P., 1991. Le Cisaillement Centre Camerounais. Rôle  
876 structural et géodynamique dans l'orogénèse panafricaine. Comptes rendus de  
877 l'Académie des sciences. Série 2, Mécanique, Physique, Chimie, Sciences de l'univers,  
878 Sciences de la Terre 313(4), 457-463.

879 Ngako, V., Affaton, P., Njonfang, E., 2008. Pan-African tectonic in northwestern Cameroon:  
880 Implication for history of Western Gondwana. Gondwana Research 14, 509-522.

881 Ngako, V., Affaton, P., Nnange, J.M., Njanko, Th., 2003. Pan-African tectonic evolution in  
882 central and southern Cameroon: transpression and transtension during sinistral shear  
883 movements. Journal of African Earth Sciences 36, 207-214.

884 Njonfang, E., Ngako, V., Kwekam, M., Affaton, P., 2006. Les orthogneiss calco-alcalins de  
885 Foumban–Bankim: témoins d'une zone interne de marge active panafricaine en  
886 cisaillement. Comptes Rendus Geoscience 338(9), 606-616.

887 Nomo Negue, E., Tchameni, R., Vanderhaeghe, O., Sun, F., Barbey, P., Tekoum, L., Fosso  
888 P.M., Eglinger, A., Saha Fouotsa, A.N., 2017. Structure and LA-ICP-MS zircon U-Pb  
889 dating of syn-tectonic plutons emplaced in the Pan-African Banyo-Tcholliré shear zone  
890 (Central North Cameroun). *Journal of African Earth Sciences* 131, 251-271.

891 Nsifa, E.N., Tchameni, R., Anne, N., Roberto, S., Andre, P., Jerome, B., 2013. Structure and  
892 petrology of Pan-African nepheline syenites from the South West Cameroon;  
893 Implications for their emplacement mode, petrogenesis and geodynamic significance.  
894 *Journal of African Earth Sciences* 87, 44-58.

895 Nzenti, J. P., Ngako, V., Kambou, R., Penaye, J., Bassahak, J., Njel, O. U., 1992. Structures  
896 régionales de la chaîne panafricaine du Nord-Cameroun. *Comptes rendus de*  
897 *l'Académie des sciences. Série 2, Mécanique, Physique, Chimie, Sciences de l'univers,*  
898 *Sciences de la Terre* 315 (2), 209-215.

899 Oliveira, E.P., Toteu, S.F., Araújo, M.N.C., Carvalho, M.J., Nascimento, R.S., Bueno, J.F.,  
900 McNaughton, N., Basili, G., 2006. Geologic correlation between the Neoproterozoic  
901 Sergipano belt (NE Brazil) and the Yaoundé schist belt (Cameroon, Africa). *Journal of*  
902 *African Earth Sciences* 44, 470-478.

903 Parsons, A. J., Ferré, E. C., Law, R. D., Lloyd, G. E., Phillips, R. J., Searle, M. P., 2016.  
904 Orogen-parallel deformation of the Himalayan midcrust: Insights from structural and  
905 magnetic fabric analyses of the Greater Himalayan Sequence, Annapurna-Dhaulagiri  
906 Himalaya, central Nepal. *Tectonics* 35(11), 2515-2537.

907 Passchier, C. W., and Trouw, R. A., 2005. *Microtectonics*. Springer Science and Business  
908 Media

909 Paton, C., Woodhead, J. D., Hellstrom, J. C., Hergt, J. M., Greig, A., Maas, R., 2010.  
910 Improved laser ablation U-Pb zircon geochronology through robust downhole  
911 fractionation correction. *Geochemistry, Geophysics, Geosystems*, 11(3).

912 Penaye, J., Kröner, A., Toteu, S.F., Van Schmus, W.R., Doumnang, J.C., 2006. Evolution of  
913 the Mayo-Kebbi region as revealed by zircon dating: an early (ca. 740 Ma) Pan-African  
914 magmatic arc in southwestern Chad. *Journal of African Earth Sciences* 44, 530-542.

915 Penaye, J., Toteu, S.F., Tchameni, R., Van Schmus, R.W., Tchakounté, J., Ganwa, A.A.,  
916 Minyem D., Nsifa, N.E., 2004. The 2.1 Ga West Central African belt in Cameroon:  
917 extension and evolution. *Journal of African Earth Sciences* 39(3-5), 159-164.

918 Petrus, J. A., and Kamber, B. S., 2012. Visual Age: A novel approach to laser ablation ICP-MS  
919 U-Pb geochronology data reduction. *Geostandards and Geoanalytical Research* 36(3),  
920 247-270.

921 Pirajno, F., Uysal, I., Naumov A., E., 2020. Oceanic lithosphere and ophiolites: Birth, life and  
922 final resting place of related ore deposits, *Gondwana Research* 88, 333-352.

923 Pouclet, A., Vidal, M., Doumnang, J.C., Vicat, J.P., Tchameni, R., 2006. Neoproterozoic  
924 crustal evolution in Southern Chad: Pan-African ocean basin closing, arc accretion and  
925 late- to post-orogenic granitic intrusion. *Journal of African Earth Sciences* 44, 543-560.

926 Pueyo, E. L., Román-Berdiel, M. T., Bouchez, J. L., Casas, A. M., Larrasoña, J. C., 2004.  
927 Statistical significance of magnetic fabric data in studies of paramagnetic granites.  
928 Geological Society, London, *Special Publications* 238(1), 395-420.

929 Ranjan, S., Upadhyay, D., Abhinay, K., Pruseth, K.L. and Nanda, J.K., 2018. Zircon  
930 geochronology of deformed alkaline rocks along the Eastern Ghats Belt margin: India–  
931 Antarctica connection and the Enderbia continent. *Precambrian Research* 310, 407-  
932 424

933 Rochette, P., 1987. Magnetic susceptibility of the rock matrix related to magnetic fabric  
934 studies. *Journal of Structural Geology* 9(8), 1015-1020.

935 Rochette, P., Scaillet, B., Guillot, S., Lefort, P., Pêcher, A. 1994. Magnetic properties of High  
936 Himalayan leucogranites: structural implications. *Earth and Planetary Science Letters*,  
937 126, 217–234.

938 Saha-Fouotsa, A. N., Vanderhaeghe, O., Barbey, P., Eglinger, A., Tchameni, R., Zeh, A., Fosso  
939 Tchunte, P., Nomo, E. N., 2019. The Geologic Record of the Exhumed Root of the  
940 Central African Orogenic Belt in the Central Cameroon Domain (Mbé-Sassa-Mbersi  
941 Region). *Journal of African Earth Sciences* 151, 286-314.

942 Sanderson, D. J., and Marchini, W. R. D., 1984. Transpression. *Journal of structural Geology*  
943 6(5), 449-458.

944 Sant’Ovaia, H.; Cruz, C.; Gonçalves, A.; Nogueira, P.; Noronha, F., **2024**. Deciphering Iberian  
945 Variscan Orogen Magmatism Using the Anisotropy of Magnetic Susceptibility from  
946 Granites. *Minerals* 14, 309.

947 Schwoerer, P., 1965. Notice explicative sur la feuille Garoua Est avec carte géologique de  
948 reconnaissance au 1/500000. Direction des mines et géologie. Imprimerie Nationale  
949 Yaoundé, Yaoundé, p. 49.

950 Sehsah, H., Eldosouky, A.M., El Afandy, A.H., 2019. Unpaired ophiolite belts in the  
951 Neoproterozoic Allaqi-Heiani Suture, the Arabian-Nubian Shield: Evidences from  
952 magnetic data. *Journal of African Earth Sciences* 156, 26-34.

953 Sep Nlomngan, J. P., Owona, S., Pénaye, J., Tchameni, R., Moussango Ibohn, P. A., Nsifa  
954 Nkonguin, E., Toteu Sadrack, F., 2021. Tectonics and LA-ICP-MS U–Pb zircon  
955 geochronology of the Boula Ibi Region (Northern Cameroon Pan-African Orogenic  
956 Belt). *Arabian Journal of Geosciences* 14, 1-24.

957 Shao, T., Xia, Y., Ding, X., Cai, Y., Song, M., 2020. Zircon saturation model in silicate melts: a  
958 review and update. *Acta Geochimica* 39,387- 403.

959 Sheikh, J. M., Patel, S. C., Champati, A. K., Madhavan, K., Behera, D., Naik, A., Gerdes, A.,  
960 2020. Nepheline syenite intrusions from the Rengali Province, eastern India:  
961 Integrating geological setting, microstructures, and geochronological observations on  
962 their syn-tectonic emplacement. *Precambrian Research* 346, 105802.

963 Shellnutt, J.G., Yeh, M.W., Pham, N.H.T., Lee, T.Y., 2019. Cryptic regional magmatism in the  
964 southern Saharan Metacraton at 580 Ma. *Precambrian Research* 332, 105398.

965 Sláma, J., Košler, J., Condon, D. J., Crowley, J. L., Gerdes, A., Hanchar, J. M., Whitehouse, M.  
966 J., 2008. Plešovice zircon- a new natural reference material for U–Pb and Hf isotopic  
967 microanalysis. *Chemical Geology* 249(1-2), 1-35.

968 Soba, D., Michard, A., Toteu, S. F., Norman, D. I., Penaye, J., Ngako, V., 1991. Données  
969 géochronologiques nouvelles (Rb-Sr, U-Pb et Sm-Nd) sur la zone mobile panafricaine  
970 de l'Est du Cameroun: âge protérozoïque supérieur de la série de Lom. *Comptes*  
971 *rendus de l'Académie des sciences. Série 2, Mécanique, Physique, Chimie, Sciences de*  
972 *l'univers, Sciences de la Terre* 312(12), 1453-1458.

973 Sokol, K., Halama, R., Meliksetian, K., Savov, I.P., Navasardyan, G., Sudo, M., 2018. Alkaline  
974 magmas in zones of continental convergence: The Tezhsar volcano-intrusive ring  
975 complex, Armenia. *Lithos* (320-321), 172-191.

976 Szymanowski, D., Fehr, M. A., Guillong, M., Coble, M. A., Wotzlaw, J. F., Nasdala, L.,  
977 Schönbächler, M., 2018. Isotope-dilution anchoring of zircon reference materials for  
978 accurate Ti-in-zircon thermometry. *Chemical Geology* 481, 146-154.

979 Tchakounté, J., Eglinger, A., Toteu, S.F., Zeh, A., Nkoumbou, C., MvondoOndoa, J., Penaye,  
980 J., de Wit, M., Barbey, P., 2017. The Adamawa Yadé domain, a piece of Archaean crust

981 in the Neoproterozoic Central African Orogenic belt (Bafia area, Cameroon).  
982 Precambrian Research 299,210-229

983 Tchameni, R., Pouclet, A., Penaye, J., Ganwa, A.A., Toteu, S.F., 2006. Petrography and  
984 geochemistry of the Ngaoundéré Pan-African granitoids in Central North Cameroon:  
985 Implications for their sources and geological setting. Journal of African Earth Sciences  
986 44(4-5), 511-529.

987 Tchameni, R., Sun, F., Dawai, D., Danra, G., Tékoum, L., Nomo Negue, E., Dagwai, N., 2016.  
988 Zircon dating and mineralogy of the Mokong Pan-African magmatic epidote-bearing  
989 granite (North Cameroon). International Journal of Earth Sciences 105, 1811-1830.

990 Tikoff, B., and Teyssier, C., 1994. Strain modeling of displacement-field partitioning in  
991 transpressional orogens. Journal of Structural Geology 16(11), 1575-1588.

992 Tomezzoli, R. N., MacDonald, W. D., Tickyj, H., 2003. Composite magnetic fabrics and S-C  
993 structure in granitic gneiss of Cerro de los Viejos, La Pampa province, Argentina.  
994 Journal of Structural Geology 25(2), 159-169.

995 Toteu, S. F., de Wit, M., Penaye, J., Drost, K., Tait, J. A., Bouyo, M. H., Doucouré, M., 2022.  
996 Geochronology and correlations in the Central African Fold Belt along the northern  
997 edge of the Congo Craton: New insights from U-Pb dating of zircons from Cameroon,  
998 Central African Republic, and south-western Chad. Gondwana Research 107, 296-324.

999 Toteu, S. F., Penaye, J., Djomani, Y. P., 2004. Geodynamic evolution of the Pan-African belt  
1000 in central Africa with special reference to Cameroon. Canadian Journal of Earth  
1001 Sciences 41(1), 73-85.

1002 Toteu, S.F., Penaye, J., Deloule, E., Van Schmus, W.R., Tchameni, R., 2006. Diachronous  
1003 evolution of volcano-sedimentary basins north of the Congo craton: insights from U-Pb

1004 ion microprobe dating of zircons from the Poli, Lom and Yaoundé groups (Cameroon).  
1005 Journal of African Earth Sciences 44, 428-442.

1006 Toteu, S.F., Van Schmus, W.R., Penaye, J., Michard, A., 2001. New U-Pb and Sm-Nd data  
1007 from north-central Cameroon and its bearing on the pre-Pan African history of central  
1008 Africa. Precambrian Research 108, 45-73.

1009 Tripathi, K., Sen, K., Dubey, A. K., 2012. Modification of fabric in pre-Himalayan granitic  
1010 rocks by post-emplacement ductile deformation: insights from microstructures, AMS,  
1011 and U-Pb geochronology of the Paleozoic Kinnaur Kailash Granite and associated  
1012 Cenozoic leucogranites of the South Tibetan Detachment zone, Himachal High  
1013 Himalaya. International Journal of Earth Sciences 101, 761-772.

1014 Trompette, R., 1997. Neoproterozoic ( $\approx$  600 Ma) aggregation of Western Gondwana: a  
1015 tentative scenario. Precambrian Research 82(1-2), 101-112.

1016 Trompette, R.R., 1994. Geology of Western Gondwana (2000-500 Ma). Pan-African-  
1017 Brasiliano aggregation of South America and Africa. Rotterdam:Balkema, 350 p.

1018 Valentin, E., Botelho, N. F., Dantas, E. L., 2020. Monte Santo suite, an example of Ediacaran-  
1019 Cambrian deformed alkaline rocks in the Araguaia Belt, Central Brazil. Implications for  
1020 Western Gondwana evolution. Lithos 366, 105552.

1021 Van Schmus, W.R., Oliveira, E.P., Da Silva Filho, A.F., Toteu, S.F., Penaye, J., Guimaraes, I.P.,  
1022 2008. Proterozoic links between the Borborema Province, NE Brazil, and the central  
1023 African Fold belt. Special Publication. In: Pankhurst, R.J., Trouw, R.A.J., de Brito Neves,  
1024 B.B., De Wit, M.J. (Eds.), West Gondwana. Pre-cenozoic Correlations across the South  
1025 Atlantic Region. Geological Society, London 294, 69-99.

1026 Vanderhaeghe, O., André-Mayer, A.S., DiONDoh, M., Eglinger, A., Ohnenstetter, M., Isseini,  
1027 M., Cuney, M., Poujol, M., Van Lichtervelde, M., 2020. Uranium mineralization

1028 associated with late magmatic ductile to brittle deformation and Na–Ca metasomatism  
1029 of the Pan-African A-type Zabili syn-tectonic pluton (Mayo-Kebbi massif, SW  
1030 Chad). *Mineralium Deposita* 56, 1297-1319.

1031 Vavra, G., Schmid, R., Gebauer, D., 1999. Internal morphology, habit and U-Th-Pb  
1032 microanalysis of amphibolite-to-granulite facies zircons: geochronology of the Ivrea  
1033 Zone (Southern Alps). *Contributions to Mineralogy and Petrology* 134, 380-404.

1034 Wacrenier Ph 1962. Carte géologique de reconnaissance des Etats d’Afrique Equatoriale,  
1035 feuille NC-33 SO E-53 SE O-54 (Moundou) au 500 000ème. IRGM. Brazzaville

1036 Wiedenbeck, M. A. P. C., Alle, P., Corfu, F. Y., Griffin, W. L., Meier, M., Oberli, F. V., Spiegel,  
1037 W., 1995. Three natural zircon standards for U-Th-Pb, Lu-Hf, trace element and REE  
1038 analyses. *Geostandards newsletter* 19(

### 1039 **Figure captions**

1040 **Figure 1.** (a) Location of regional setting of the study area (Fig. 1c ) within South America-  
1041 Africa Fit. (b) Pre-Mesozoic fit between the northern Borborema Province (NE-Brazil) and  
1042 Cameroon (*after* Caby, 1989, modified): with location of Figure 1b indicated. Cratons  
1043 Abbreviation: AM: Amazonian; ANG: Angola; CO: Congo; KA: Kalahari; PP: Paranapanema;  
1044 RP: Río de la Plata; SF: Sao-Francisco; WA: West Africa. (c) Geological sketch map of  
1045 northern Cameroon (modified from Penaye et al., 2006). ① Post-Pan-African sediments;  
1046 ② Late- to post-tectonic Pan-African granitoids; ③ Syntectonic granite; ④ Mayo-Kebbi  
1047 batholith: tonalite, trondhjemite and granodiorite; ⑤ medium- to high-grade gneisses of  
1048 the NW-Cameroon domain; ⑥ Mafic to intermediate complex of the Mayo-Kebbi domain  
1049 (metadiorite and gabbro-diorite) and amphibolite; ⑦ □ 730-700 Ma alkaline granite; ⑧  
1050 Neoproterozoic low- to medium-grade volcano-sedimentary sequences of the Poli-Léré  
1051 Group; ⑨ Remobilized Palaeoproterozoic Adamawa-Yadé domain; ⑩ Thrust front; ⑪

1052 Strike slip fault: TBSZ: Tcholliré-Banyo shear zone; GGSZ: Godé-Gormaya shear zone; MNSZ:  
1053 Mayo-Nolti Shear Zone<sup>⑫</sup> National state border.

1054

1055 **Figure 2.** Satellite view of the Balda massif (Source: Google Earth, 03/05/2023).

1056

1057 **Figure 3.** Fields photographs of Balda granite. (a) Partial view of the eastern flank of the  
1058 Balda Massif. (b) Outcrop as slabs and blocks. (c) Quartz veins intersecting the aegyrine-  
1059 riebeckite granite. (d) Aegyrine-riebeckite granite sample with macroscopic mineral-  
1060 preferred orientation (the arrow indicates the direction of the foliation). (e) Aegyrine-  
1061 riebeckite granite sample without macroscopic mineral-preferred orientation. (f)  
1062 Leucogranite.

1063

1064 **Figure 4.** Photomicrographs of representative specimens from the Balda granite. (a)  
1065 Heterogranular textures of aegyrine-riebeckite granite and (b) leucogranite. (c) Perthitic  
1066 feldspars in the aegyrine-riebeckite granite. (d) Preferred orientation of aggregates of Mg-  
1067 Fe silicates and opaque minerals that define a foliation plane. (e) Mg-Fe silicates (aegyrine,  
1068 riebeckite, and biotite) with preferred orientation. (f) Titanite and coarse opaque minerals  
1069 showing aureole of titanite in the leucogranite. Cross-polarized light (a, b, and c) and plane  
1070 polarized light (d, e and f). Mineral abbreviations: Qtz: quartz; Kfs: K-feldspar; Bt: biotite;  
1071 Rie: Riebeckite; Aeg: aegyrine; Op: opaque minerals; Ti: titanite.

1072

1073 **Figure 5.** Spatial distribution of (a) AMS sampling stations and (b) Magnetic  
1074 Susceptibility(Km) values

1075 **Figure 6.** Correlation between AMS scalar parameters in Balda Granite: (a) Anisotropy  
1076 Percent (P %) vs. magnetic Susceptibility (Km). (b) Shape Parameter (T) vs. P%.

1077 **Figure 7.** (a) Distribution map of the anisotropy degree percentage (P %) and (b) the Shape  
1078 parameter (T) of the Balda granite.

1079 **Figure 8.** Structures in the Balda granite and in regional scale (a) Map of magnetic foliations  
1080 and orientation diagram of the poles (Schmidt, lower hemisphere and equal-area  
1081 projections; Balda granite (solid green circle):  $n = 25$ , best pole (red star):  $127^\circ/4^\circ$ ; Regional  
1082 foliation (open circle; data from Dumort and Peronne, 1966) :  $n = 18$ , best pole (black  
1083 triangle) :  $297^\circ/4^\circ$ ), (b) Map of magnetic lineation and orientation diagram of their pole  
1084 (Schmidt, lower hemisphere and equal-area projections:  $n = 25$ , best line (blue star):  
1085  $214^\circ/16^\circ$  (azimuth/plunge).

1086 **Figure 9.** Thermomagnetic curves illustrating the presence of magnetite for three  
1087 representative samples (a) BA7, (b) BA16, and (c) BA18 of the Balda granite.

1088 **Figure 10.** Photomicrographs of microstructures and kinematic markers of Balda granite.  
1089 (a) Recrystallized grains of quartz with triple joints at  $120^\circ$  (site BA2). (b) Irregular quartz-  
1090 quartz boundaries (site BA3) and (c) lobed quartz-feldspar boundaries illustrating  
1091 recrystallization by the GBM process (site BA7). (d) Bands of recrystallized grain with  
1092 elongate shape (site BA25). (e) C/S structure illustrates by elongate quartz grains (S) and  
1093 polycrystalline quartz ribbons (site BA22). (f)  $\delta$ -type mantled porphyroclast of opaque  
1094 mineral (site BA21). (g) Internally recrystallized porphyroclast illustrating recrystallization  
1095 by progressive subgrain rotation (site BA11). (h) Riebeckite fish (site BA21). (e) – (h)  
1096 Sinistral shear sense indicators. Cross-polarized light (a, b, c, d, e and g) and plane polarized  
1097 light (f and h).

1098 **Figure 11.** Chemical composition variations in “bright” vs. “dark” Zircons from Balda  
1099 Granite. (a) & (b) Trace element variations; (c) Chondrite-normalized REE Patterns.

1100 **Figure 12.** Concordia diagrams (a–d) presenting LA-ICP-MS U–Pb results of zircon grains  
1101 from Balda granite. Red shaded ellipses represent analyses from “dark” zircons. Green  
1102 shaded ellipses are data points used to calculate Concordia ages.

1103 **Figure 13.** Proposed geodynamic evolution model for the northern portion of the CAOB. a)  
1104 Early stage (ca. >800 Ma): Subduction of oceanic crust beneath the continental crust of the  
1105 Mayo-Kebbi domain led to the formation of a magmatic arc. b) Back-arc basin development  
1106 (ca. 730 Ma): The subduction event was followed by the development of a back-arc basin,  
1107 accompanied by the emplacement of tholeiitic gabbros and alkaline granites. c) Continental  
1108 collision initiation (ca. 680 Ma): The model suggests the initiation of continental collision  
1109 between the North-West Cameroon and Mayo-Kebbi domains around 680 Ma.

1110

### 1111 **Table captions**

1112 **Table 1.** Anisotropy of magnetic susceptibility (AMS) data for the Balda pluton. n: number  
1113 of specimens analyzed in each site;  $K_m$  : mean magnetic susceptibility;  $K1D^\circ$ ,  $K3D^\circ$ :  
1114 declination of K1 and K3, respectively;  $K1I^\circ$ ,  $K3I^\circ$ : inclination of K1 and K3, respectively ;  
1115  $E12$ ,  $E31$ : 95% confidence angles for the long (1) and short (3) axes of the magnetic  
1116 susceptibility ellipsoid; P%: anisotropy percentage of the magnetic susceptibility; T: shape  
1117 parameter.

1118

1119 **Table 2.** LA-ICP-MS U-Pb isotopic data of analyzed zircon from the Balda granite. 2SE: 2-  
1120 sigma standard error

1121 **Table 3.** Trace element composition (ppm) of analyzed zircons from the Balda granite

1122 **Supplementary material**

1123 **Supplementary Table 1.** LA-ICP-MS U-Pb isotopic and trace element analyses on zircon -

1124 Metadata

1125 **Supplementary Figure 1.** Cathodoluminescence (CL) images of selected zircons crystals

1126 from the Balda granite.

1127

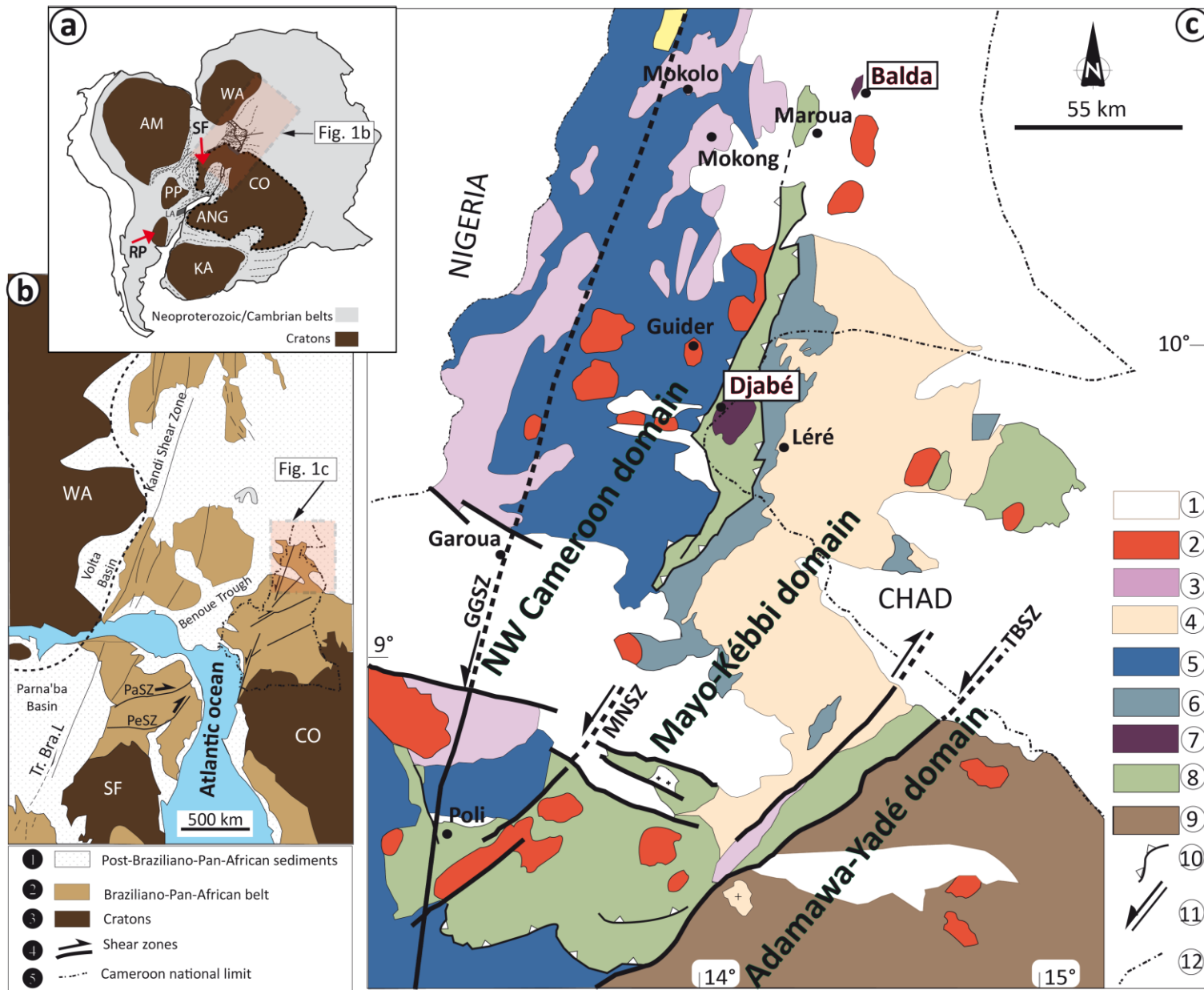


Figure 1.



Figure 2.

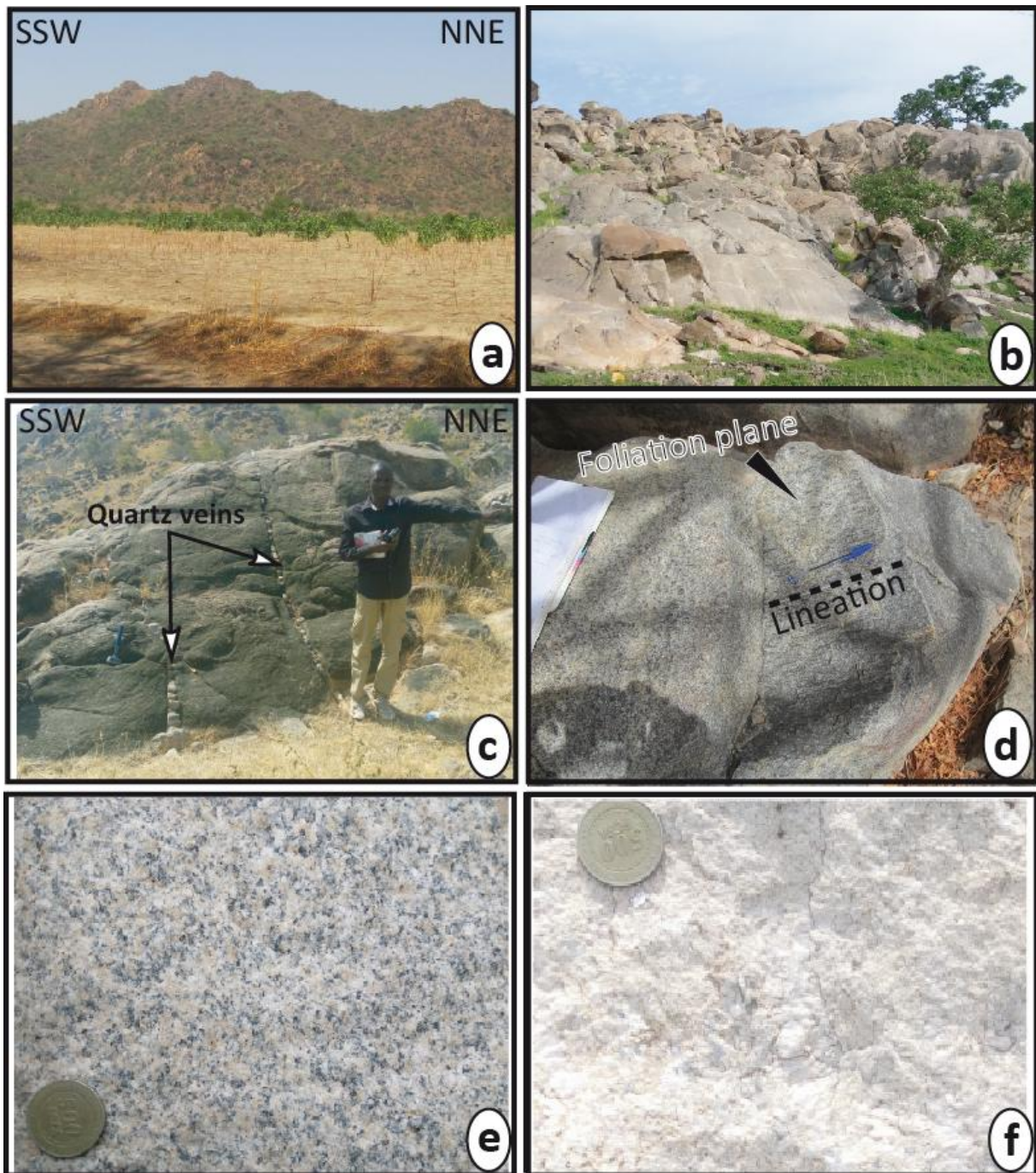


Figure 3.

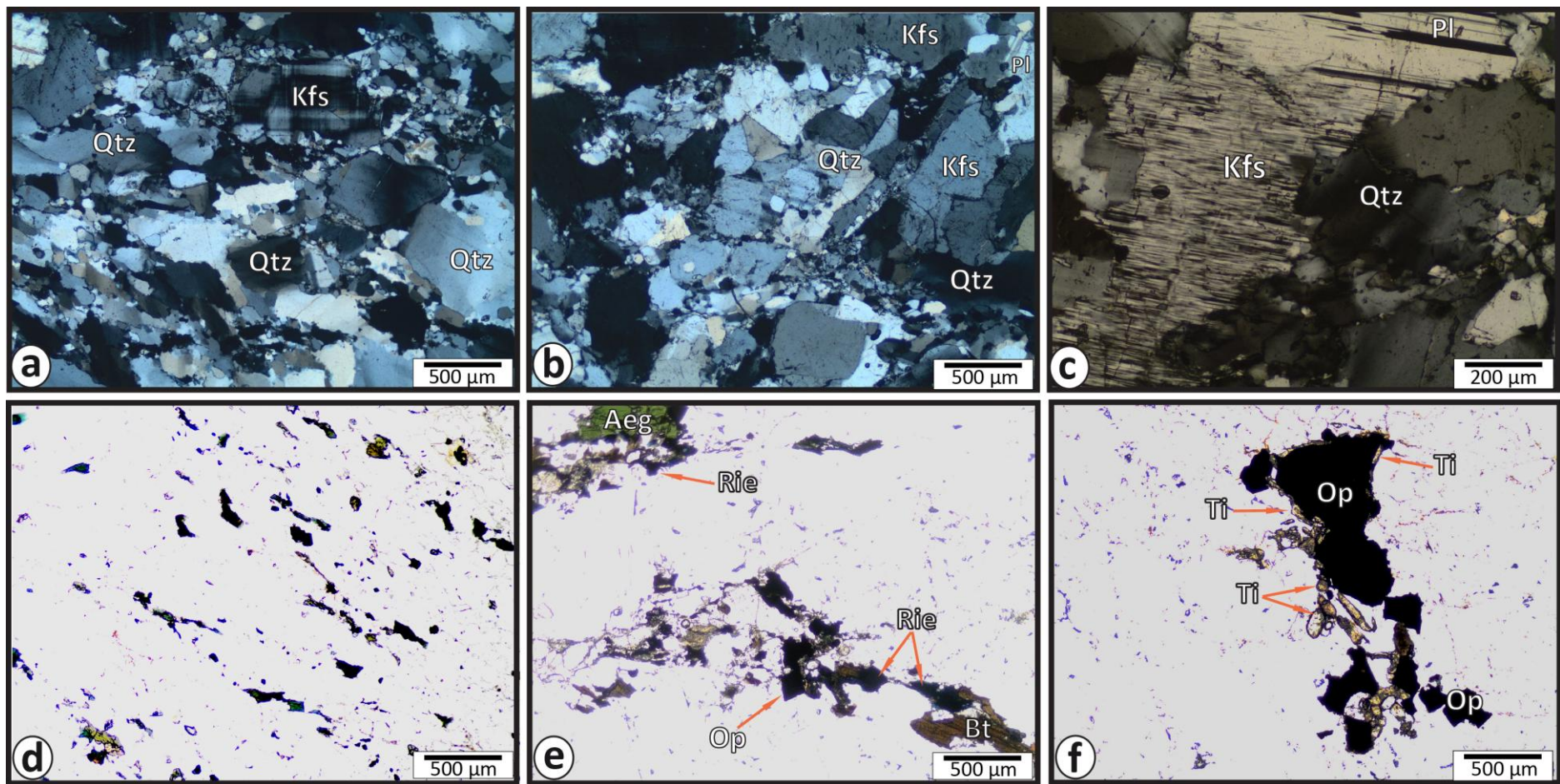


Figure 4.

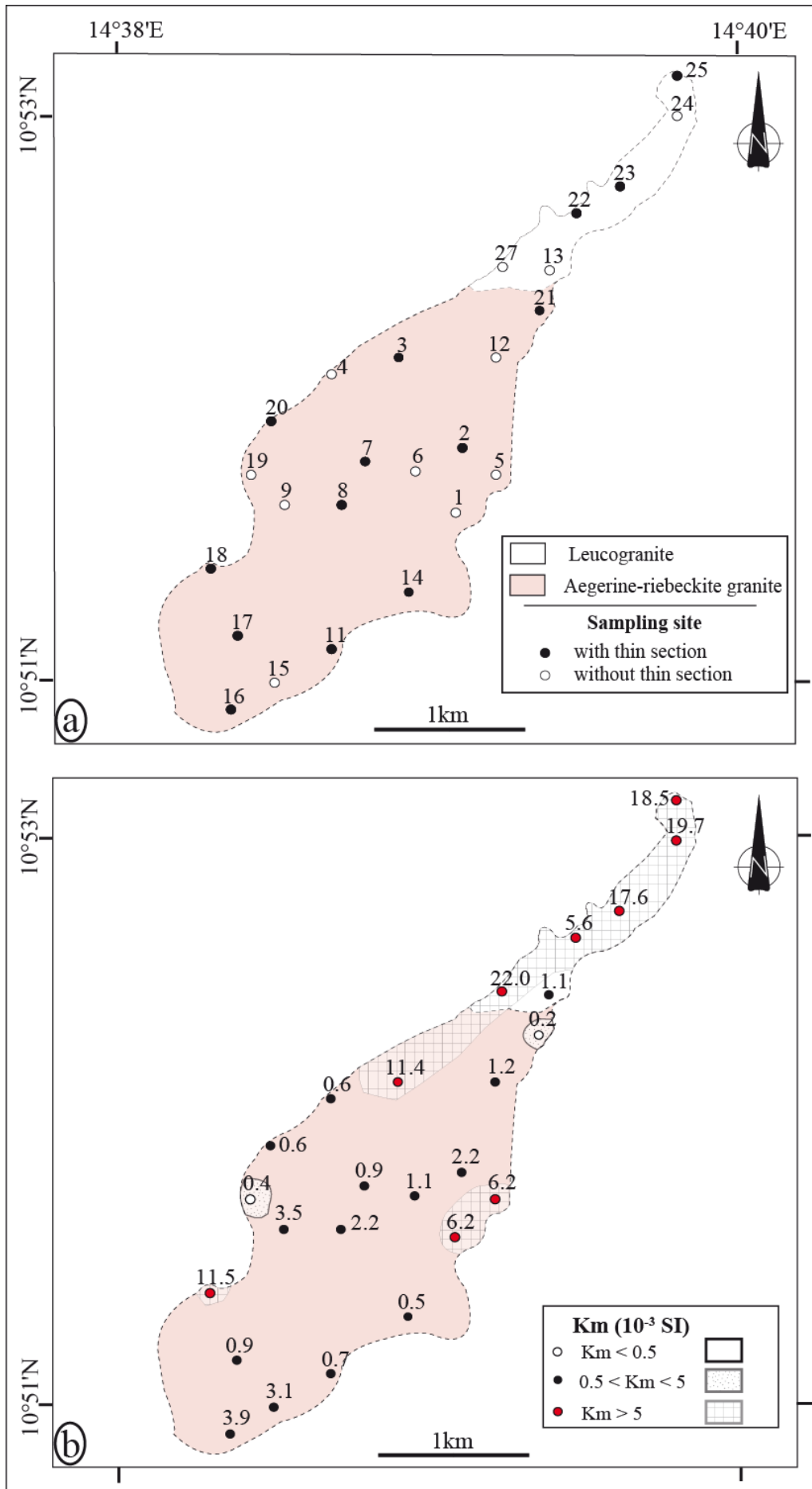
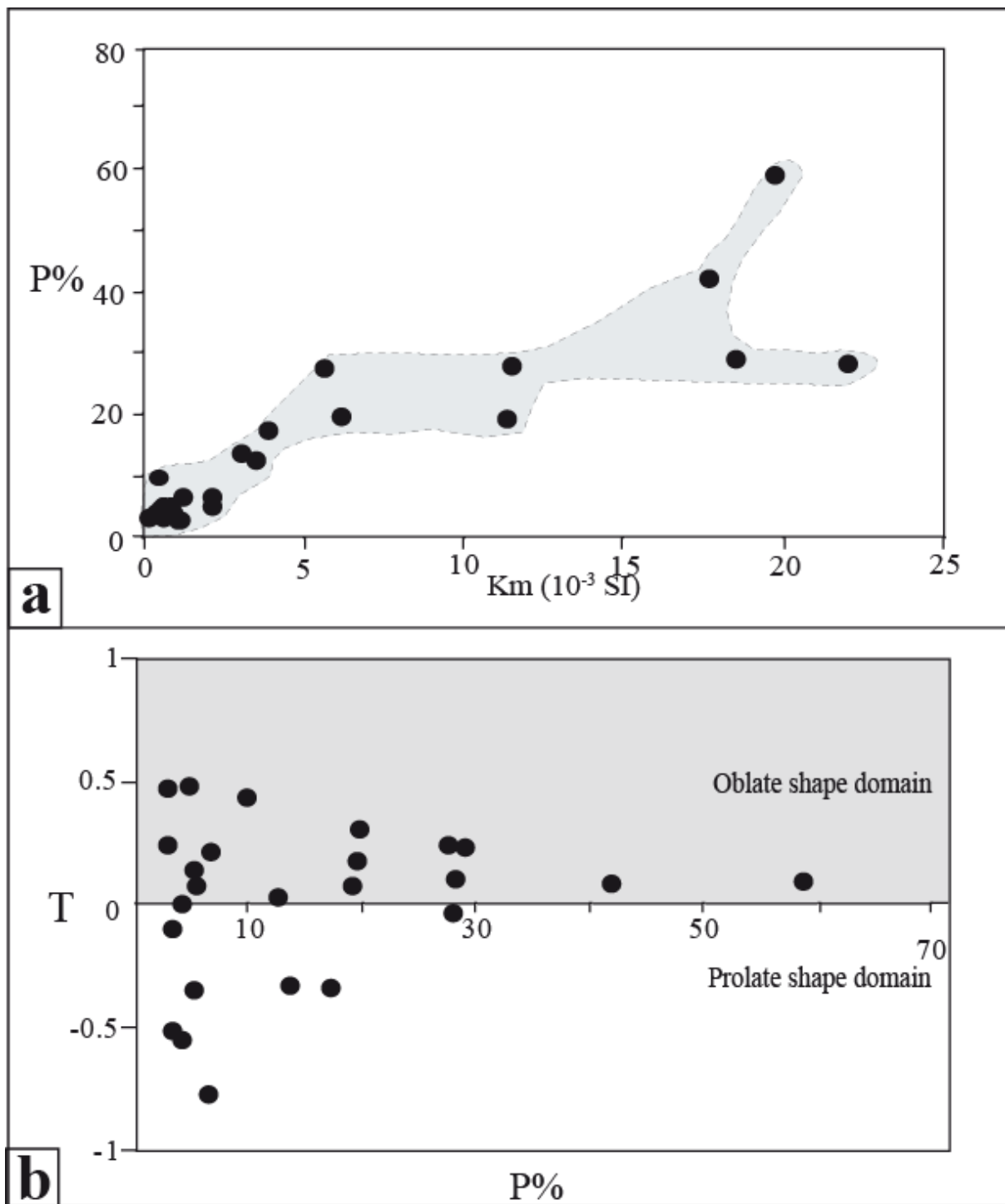


Figure 5.



Figure

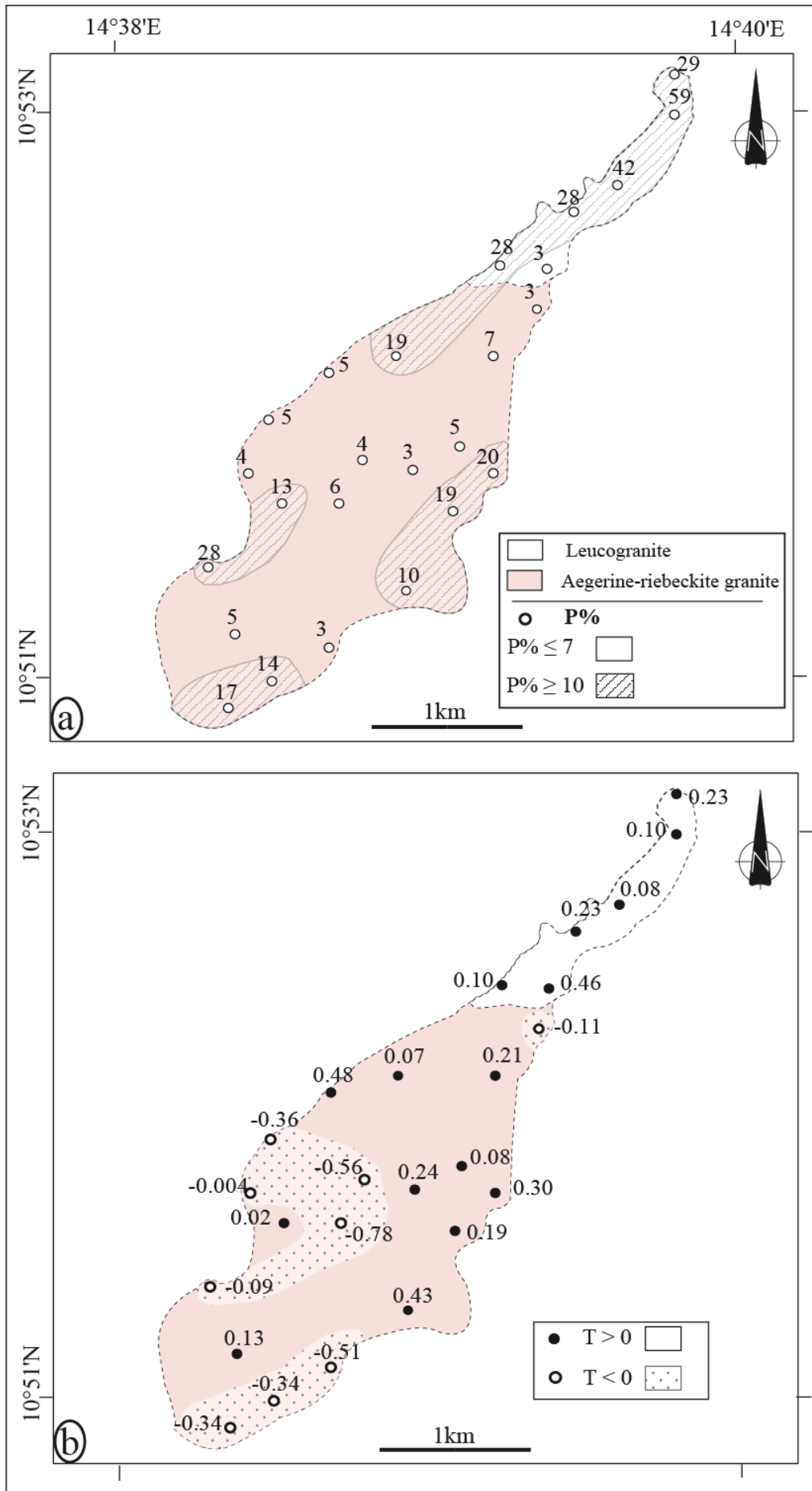


Figure 7.

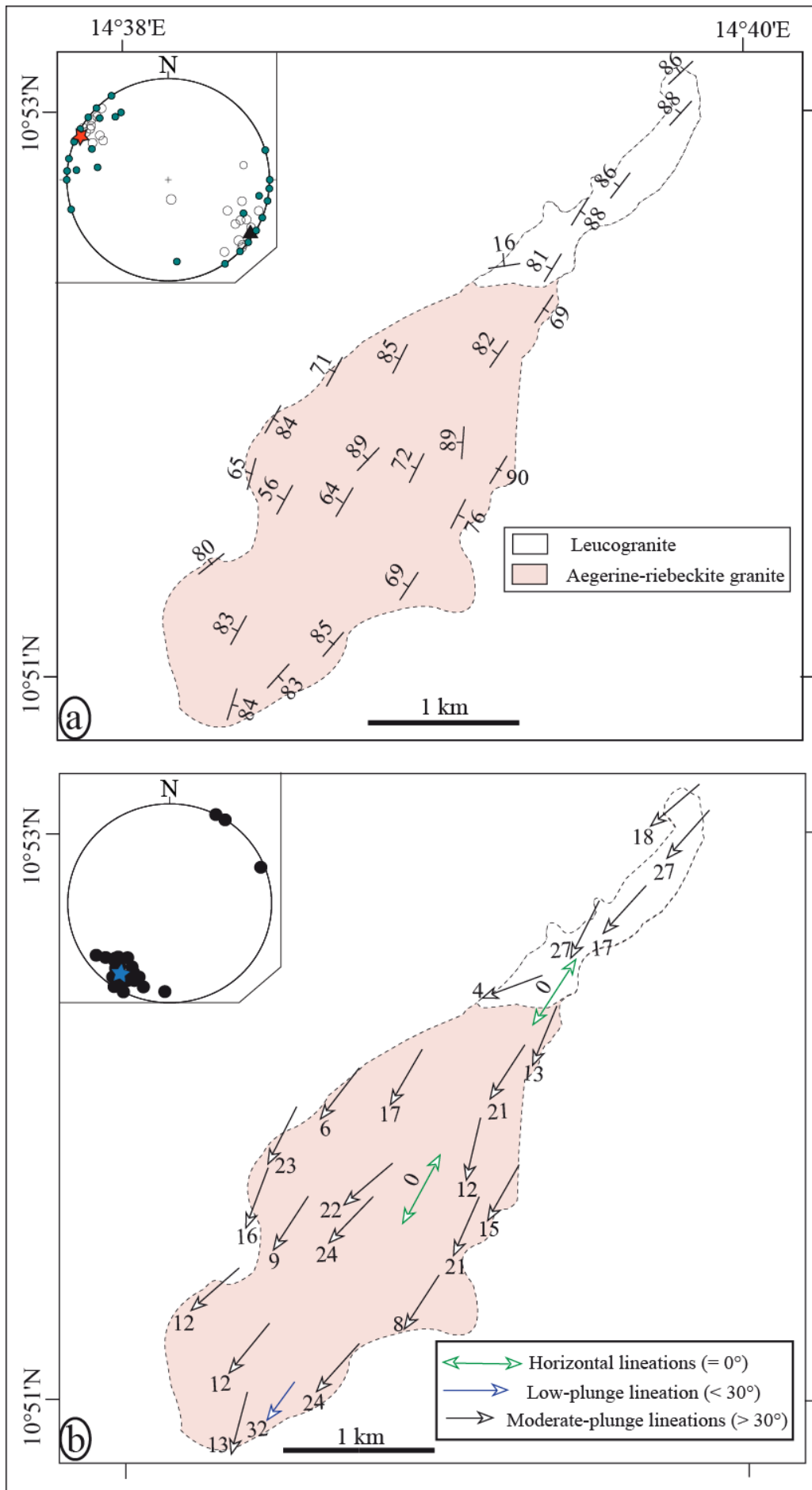


Figure 8.

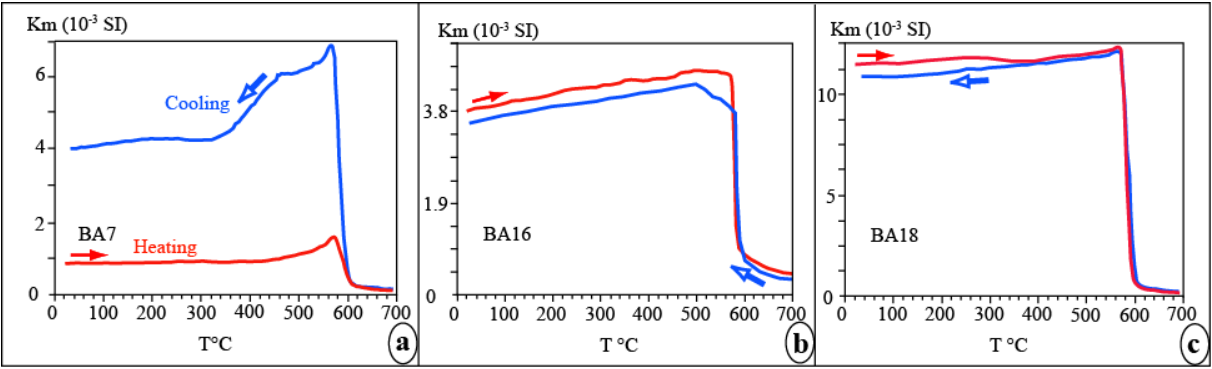


Figure 9.

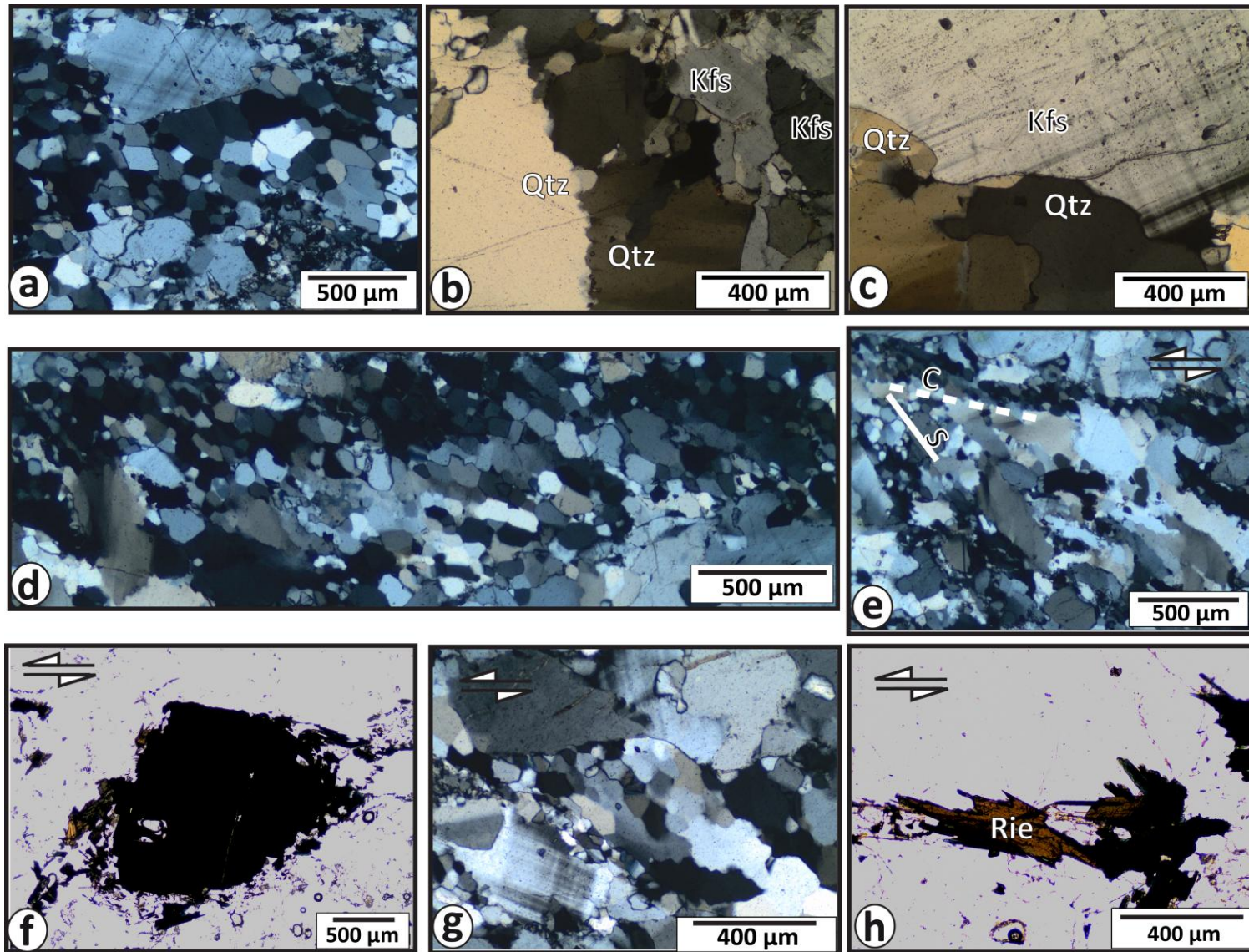


Figure 10.

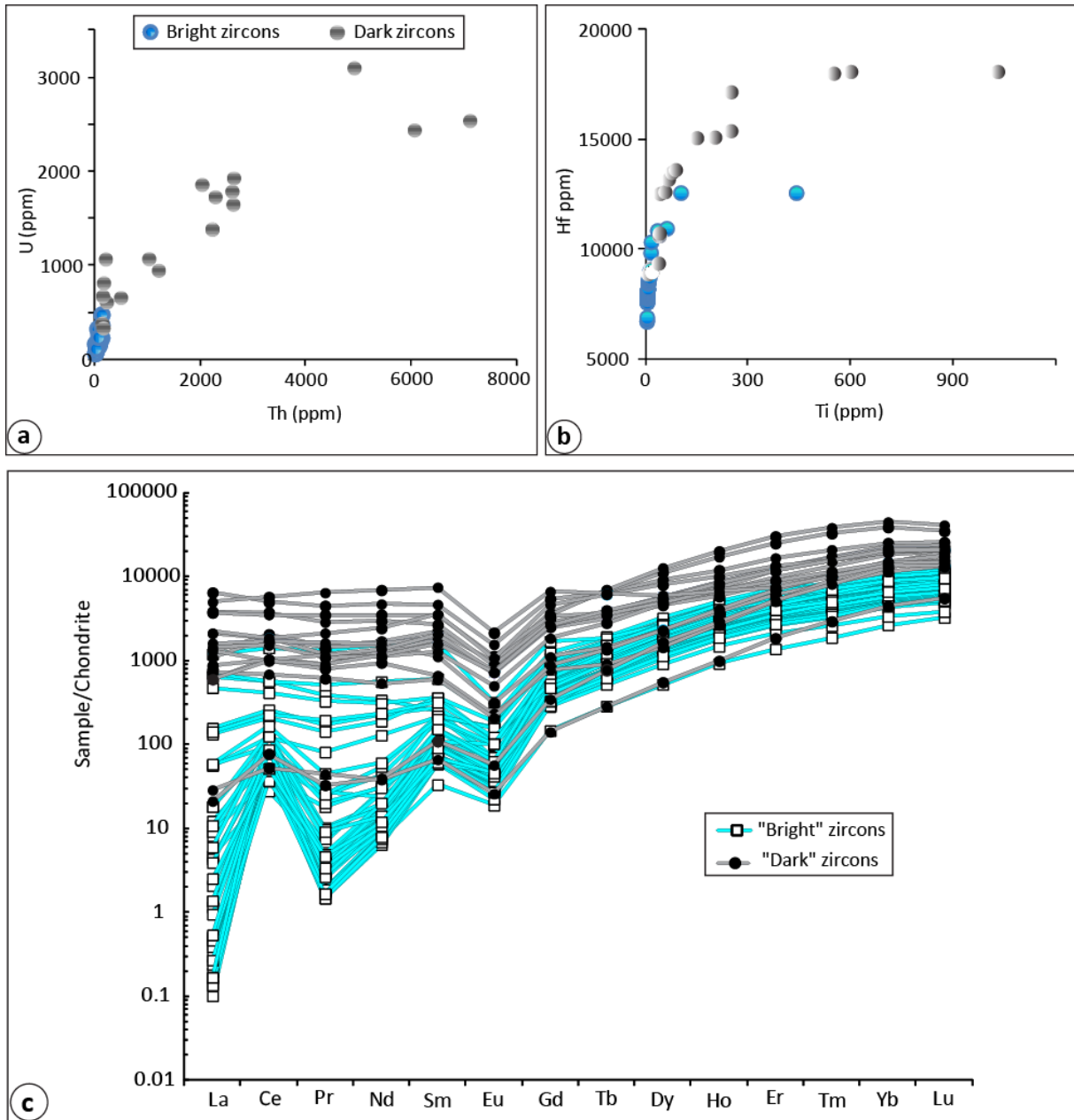


Figure 11.

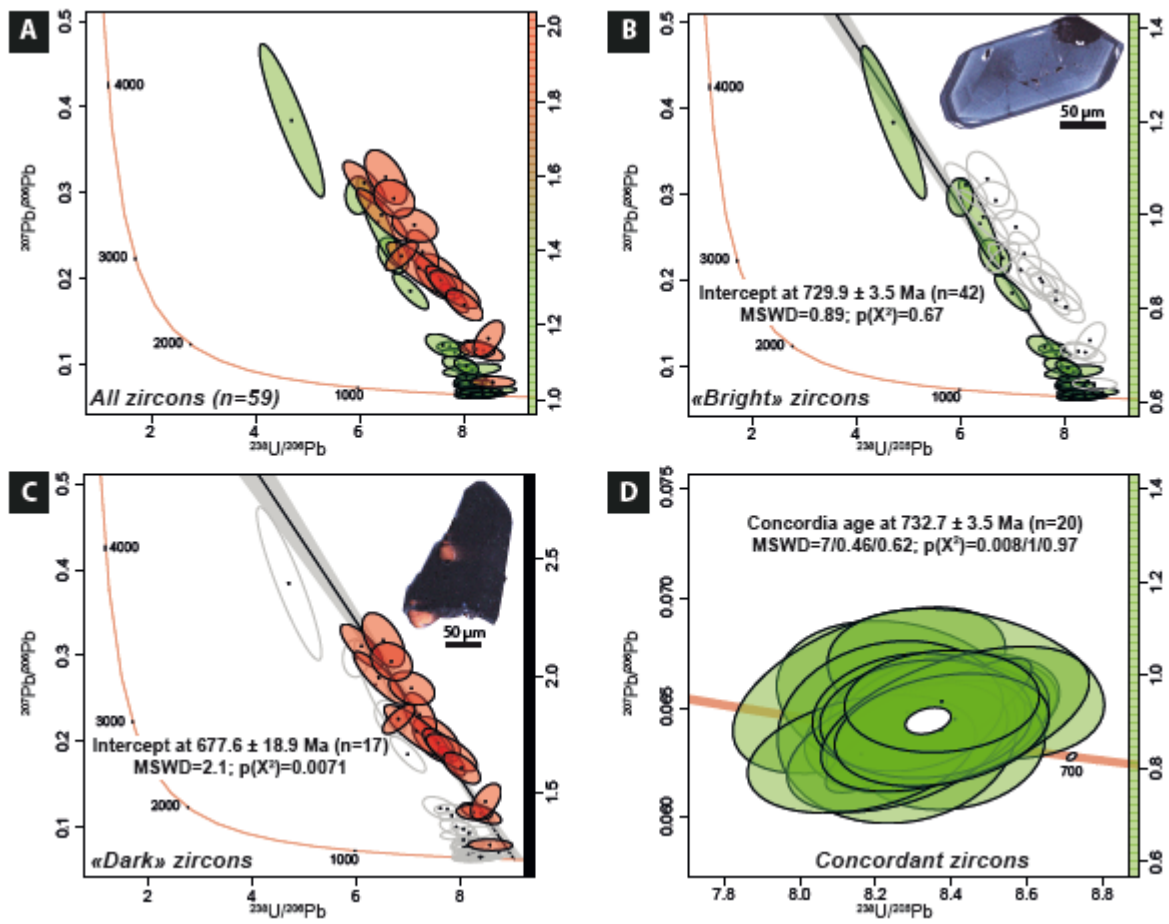


Figure 12.

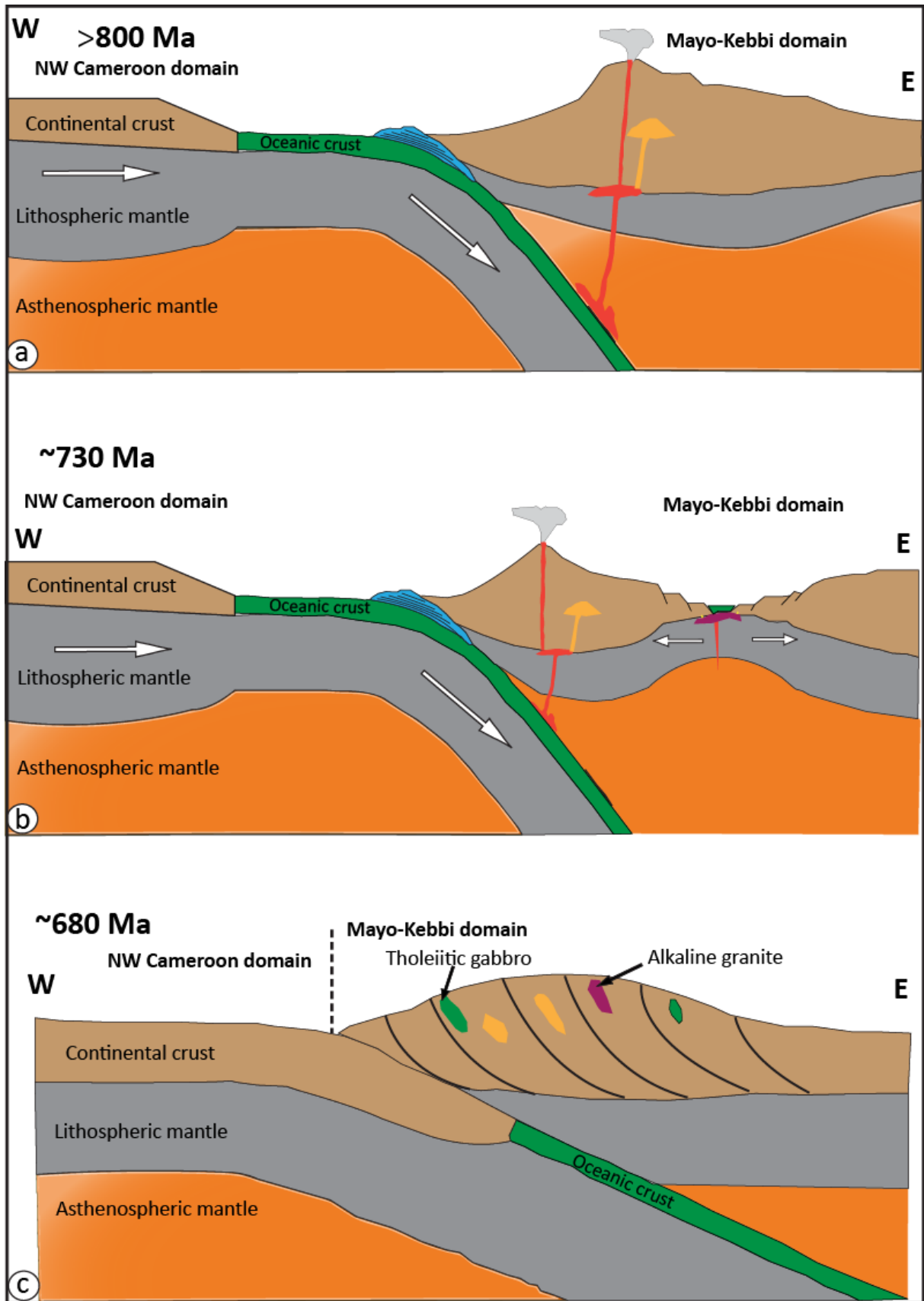


Figure 12.